Cellular/Molecular

USP1/UAF1-Stabilized METTL3 Promotes Reactive Astrogliosis and Improves Functional Recovery after Spinal Cord Injury through m^{6}A Modification of YAP1 mRNA

Xuhui Ge,[1*] Wu Ye,[1*] Yufeng Zhu,[1*] Min Cui,[3] Jiawen Zhou,[4] Chenyu Xiao,[3] Dongdong Jiang,[5] Pengyu Tang,[1] Jiaxing Wang,[1] Zhuanghui Wang,[1] Chengyue Ji,[1] Xuhui Zhou,[2] Xiaojian Cao,[1] Wei Liu,[2] and Weihua Cai[1]

[1]Department of Orthopedics, The First Affiliated Hospital of Nanjing Medical University, Nanjing, Jiangsu 210029, China, [2]Department of Orthopedics, Second Affiliated Hospital of Naval Medical University, Shanghai 200003, China, [3]Department of Human Anatomy, Nanjing Medical University, Nanjing, Jiangsu 211166, China, [4]Department of Pharmacology, China Pharmaceutical University, Nanjing 211198, China, and [5]Department of Orthopedics, Nanjing First Hospital, Nanjing Medical University, Nanjing, Jiangsu 210006, China

RNA N^6-methyladenosine (m^{6}A) modification is involved in diverse biological processes. However, its role in spinal cord injury (SCI) is poorly understood. The m^{6}A level increases in injured spinal cord, and METTL3, which is the core subunit of methyltransferase complex, is upregulated in reactive astrocytes and further stabilized by the USP1/UAF1 complex after SCI. The USP1/UAF1 complex specifically binds to and subsequently removes K48-linked ubiquitination of the METTL3 protein to maintain its stability after SCI. Moreover, conditional knockout of astrocytic METTL3 in both sexes of mice significantly suppressed reactive astrogliosis after SCI, thus resulting in widespread infiltration of inflammatory cells, aggravated neuronal loss, hampered axonal regeneration, and impaired functional recovery. Mechanistically, the *YAP1* transcript was identified as a potential target of METTL3 in astrocytes. METTL3 could selectively methylate the 3′-UTR region of the *YAP1* transcript, which subsequently maintains its stability in an IGF2BP2-dependent manner. *In vivo*, YAP1 overexpression by adeno-associated virus injection remarkably contributed to reactive astrogliosis and partly reversed the detrimental effects of METTL3 knockout on functional recovery after SCI. Furthermore, we found that the methyltransferase activity of METTL3 plays an essential role in reactive astrogliosis and motor repair, whereas METTL3 mutant without methyltransferase function failed to promote functional recovery after SCI. Our study reveals the previously unreported role of METTL3-mediated m^{6}A modification in SCI and might provide a potential therapy for SCI.

Key words: **METTL3; reactive astrogliosis; spinal cord injury; USP1/UAF1; YAP1**

Significance Statement

Spinal cord injury is a devastating trauma of the CNS involving motor and sensory impairments. However, epigenetic modification in spinal cord injury is still unclear. Here, we propose an m^{6}A regulation effect of astrocytic METTL3 following spinal cord injury, and we further characterize its underlying mechanism, which might provide promising strategies for spinal cord injury treatment.

Introduction

Spinal cord injury (SCI) is a devastating trauma of the CNS involving motor and sensory impairment. The global morbidity rate of SCI is 10.5 cases per 100,000 people (Kumar et al., 2018), which poses a great burden on individuals and the health care system. Despite extensive studies on therapies for SCI, the transfer from basic to clinical research is still limited (James et al., 2018). Pathophysiologically, primary injury of the spinal cord is mainly caused by physical force, followed by a progressive secondary injury that is characterized by blood–spinal cord barrier disruption, tissue edema, and neuronal apoptosis (Tran et al., 2018). Therefore, there is an urgent need for a better understanding of the cellular response after SCI and its underlying molecular mechanisms.

Received June 20, 2022; revised Jan. 1, 2023; accepted Jan. 11, 2023.

Author contributions: W.C. and X.G. designed research; X.G., W.Y., M.C., J.Z., C.X., and W.L. performed research; X.Z. and X.C. contributed unpublished reagents/analytic tools; W.C., X.G., W.Y., Y.Z., J.Z., C.X., D.J., P.T., J.W., Z.W., C.J., X.C., and W.L. analyzed data; W.C., X.G., and W.L. wrote the paper.

This work was supported by National Natural Science Foundation of China Grants 81974335 and 82172426. We thank the Core Facility of the First Affiliated Hospital of Nanjing Medical University for help with the experiment.

*X.G., W.Y., and Y.Z. contributed equally to this work.

The authors declared no competing financial interests.

Correspondence should be addressed to Weihua Cai at caiwhspine@sina.com or Wei Liu at weiliuspine@sina.com or Xiaojian Cao at xiaojiancao001@163.com.

https://doi.org/10.1523/JNEUROSCI.1209-22.2023

Astrocytes, the most numerous glial cells in the CNS, play essential roles in various neurologic diseases, including acute trauma and degeneration disorders (Li et al., 2020). In injured spinal cords, astrocytes adjacent to the lesion undergo a specific cellular change known as reactive astrogliosis, which is characterized by proliferation and hypertrophy, as well as a morphologic increase in protrusion length (Vivinetto et al., 2020). The reactive astrogliosis process in CNS injury has similarities with wound healing in other non-neural tissues, including cytoskeletal remodeling, cell junction degradation, and mesenchymal characteristic acquirement, as well as extensive changes in gene expression. Previous studies demonstrated that in addition to repairing the blood–spinal cord barrier and attenuating oxidative stress, reactive astrocytes adjacent to lesions organized to form a dense boundary that walled off the epicenter and protected surrounding tissues (Pekny and Pekna, 2014; Vivinetto et al., 2020). Another study indicated that astrocyte activation and astrocyte scar formation could contribute to axon regeneration after SCI (Anderson et al., 2016). Although extensive studies have unveiled the mechanism of reactive astrogliosis, the epigenetic modification within reactive astrocytes and its role in SCI are still unclear.

As the most abundant internal mRNA modification, N^6-methyladenosine (m^{6}A) has garnered more and more attention in recent years (Zaccara et al., 2019). This post-transcriptional modification is reversibly modulated near stop codons and in the 3′-UTR region of transcripts by a specific set of enzymes known as m^{6}A writer, eraser, and reader. Generally, the formation of m^{6}A is catalyzed by a core methyltransferase complex (METTL3, METTL14, and WTAP) and can be reversed by demethylases FTO (fat mass and obesity-associated) and ALKBH5 (Yang et al., 2018a). In addition to WTAP, other binding partners including RBM15 and its paralogue RBM15B exert similar functions in methyltransferase processes through binding and recruiting METTL3 and METTL14 to specific sites in mRNA (Patil et al., 2016). The mRNA methylated in selective consensus motif RRACH (where R = G/A, H = A/C/U) is recognized and regulated by different reader proteins. It has been reported extensively that m^{6}A modification participates in the regulation of pre-mRNA splicing in the nucleus and mRNA export, initiation, translation, and decay processes in the cytoplasm depending on the functions of the reader protein (Lin et al., 2019; Shen et al., 2020). For instance, YTHDF1 preferentially promotes mRNA translation by interacting with translation initiation factors; YTHDF2/3 and YTHDC1 are mainly responsible for facilitating mRNA degradation, whereas the IGF2BP family maintains stability of target transcripts (Shi et al., 2019). This phenomenon might be determined by different recognition sites or competitive binding for shared targets. Most previous studies have documented that m^{6}A modification is involved in various biological and pathologic events, including stem cell self-renewal, sex determination, early embryonic development, and cancer progression (Lence et al., 2016; Zhao et al., 2017; Y. Wang et al., 2018). In terms of the CNS, the great majority of previous studies have focused on the roles of m^{6}A modification in neural development and axonal generation in nontraumatic diseases (Yoon et al., 2017; C.X. Wang et al., 2018; Yu et al., 2018), whereas its functions after SCI have not been recognized.

In the present study, we noted an increased level of m^{6}A in injured spinal cords and demonstrated that the METTL3 protein was upregulated after SCI and further stabilized by the USP1/UAF1 complex, thus subsequently promoting reactive astrogliosis, blocking infiltration of inflammatory cells, and improving functional recovery through modulating methylation and stability of *YAP1* transcript in an IGF2BP2-dependent manner. In sum, our study proposes the epigenetic regulation of astrocytic METTL3 following SCI and uncovers its underlying mechanism, which might offer promising strategies for SCI treatment.

Materials and Methods

Animals

The Mettl3$^{fl/fl}$ and GFAP-Cre mice with C57BL/6 background were generated at Cyagen Biosciences. The astrocyte-conditional knock-out mice were produced by crossing Mettl3$^{fl/fl}$ and GFAP-Cre mice, and genotype identification was performed postnatally. All mice were housed under a 12 h light/dark cycle with appropriate humidity and temperature and provided with food and water *ad libitum*. All procedures were conducted under the approval of the Animal Committee of the First Affiliated Hospital of Nanjing Medical University.

SCI model and treatment

The contusive SCI model was performed in mice of both sexes as described in our previous study (Ge et al., 2021). Briefly, mice were anesthetized by isoflurane inhalation, and T8-level laminectomy was subsequently performed to expose the spinal cord. Dorsal injury of the cord was made by dropping a rod (5 g) from a height of 6.5 cm using a spinal cord impactor (68097, RWD). After hemostasis, the muscles and skin were sutured hierarchically. The bladder was auxiliary evacuated twice daily until the urinating function was restored. The mice in the sham group were subjected to T8-level laminectomy alone.

Adeno-associated virus infection

To specifically express exogenous METTL3 or YAP1 in astrocytes *in vivo*, pAAV9-GfaABC$_1$D-3×Flag-WPRE carrying mouse *METTL3* cDNA sequence [adeno-associated virus (AAV)-METTL3-WT], or *METTL3* cDNA sequence with methyltransferase domain-mutated (AAV-METTL3-MUT), and pAAV9-GfaABC$_1$D-3×Flag-WPRE carrying mouse *YAP1* cDNA sequence (AAV-YAP1) were constructed (Obio Technology). The pAAV9-GfaABC$_1$D-MCS-WPRE (Obio Technology) served as a negative control. An injection was performed (5×10^9 vg, 1 µl) immediately after SCI using a syringe pump connected to a 10 µl Hamilton syringe at a rate of 200 nl/min into the cranial and caudal spinal cord of lesion sites at a depth of 1 mm. The syringe was kept in place for an additional 5 min after injection to allow viral diffusion.

Behavioral analysis

The motor and sensory functions of mice were assessed at 1, 3, 7, 14, and 28 d postinjury.

Basso Mouse Scale behavioral analysis. The Basso Mouse Scale (BMS) score was evaluated by two investigators blinded to the groups at 1, 3, 7, 14, and 28 d postinjury according to the hindlimb locomotor function. Each mouse was individually placed in an open field, and the BMS score was evaluated from 0 to 9 based on hindlimb joint movements, trunk position and stability, stepping coordination, paw placement, toe clearance, and tail position.

Footprint analysis. Footprint analysis was used to assess the athletic ability of forelimbs and hindlimbs of mice. After the forelimbs and hindlimbs were brushed with blue and red nontoxic ink, respectively, mice were required to walk on a straight paper-lined runway, as described previously (Ge et al., 2021). The stride length and width were then measured and analyzed only when the mice ran at a constant speed.

Rotarod test. A rotarod test was performed to access the balance and motor coordination after SCI. Mice were placed on an accelerating rotarod (Shanghai XinRuan Information Technology) from 0 to 40 rpm. Each mouse was allowed to practice for one trial before the two test trials. The interval between each trial is 20 min. Time taken to fall and tolerable speed of the rotarod were averaged from two individual test trials for a final score per mouse.

Ladder walking test. For the ladder walking test, pretrained mice were placed on a horizontal ladder with regularly or irregularly placed 3 mm diameter rungs (Beijing Cinontech Co., Ltd.) at 7, 14, 21 and 28 d after SCI, and a home cage was placed at the end of the ladder. The side and bottom views of mice walking were recorded for further foot faults (drag, slips, or foot falls) calculation and hindlimb coordination analysis.

von Frey filament test. The von Frey filament test was used to evaluate the tactile sensitivity of hindlimbs after SCI. Each mouse was tested at baseline before SCI and at 28 d postinjury. Mice were placed on a metal mesh to allow access to the plantar surface of paws. The hindpaw was stimulated with a set of calibrated von Frey filaments (Yuyan Instruments). Each hindpaw received five consecutive treatments, and hindpaw withdrawal or licking was regarded as a positive response. Three positive responses of five repetitive stimuli were defined as the von Frey threshold.

Electromyography test. The motor-evoked potentials (MEPs) were examined 28 d after SCI by electromyography tests as previously described (Jiang et al., 2020). Mice were anesthetized, and the stimulation, recording, reference, and grounding electrodes were placed at the rostral ends of the spinal cord, flexor of biceps femoris, distal tendon of hindlimb muscle, and under the skin, respectively. A single stimulation (0.5 mA, 0.5 ms, 1 Hz) was used to induce MEPs, then peak-to-trough amplitude and latency (from the onset of stimulus to the first response of each wave) were quantified to determine the hindlimb nerve conduction function.

Immunofluorescence staining

Mice were killed and perfused with ice-cold PBS followed by 4% paraformaldehyde. Spinal cord samples were fixed overnight at 4°C and gradient dehydrated in 15% and 30% sucrose solutions, then embedded in optimal cutting temperature compound and dissected into 14-μm-thick sections. For spinal cord tissue immunofluorescence staining, frozen sections were washed with PBS and blocked with 5% BSA plus 0.3% Triton X-100 at room temperature for 1 h. Following incubation with diluted primary antibodies overnight at 4°C, conjugated secondary antibodies (Alexa Fluor 488 and Alexa Fluor 594, 1:200; Jackson ImmunoResearch) were subsequently added, and DAPI was used to visualize the nucleus. The images were photographed under a SLIDEVIEW VS200 digital slide scanner (Olympus). To evaluate the lesion area, a single channel image of the spinal cord was first opened by ImageJ software. After threshold modification, the lesion area was selected using a freehand section tool, and the selected area was then imported into ROI Manager. The scale was set using a wand tool, and the lesion area was subsequently measured in ROI Manager. Additionally, the number of CD68$^+$ cells and NeuN$^+$ cells was evaluated using particle analysis module after images threshold modification and cell separation. To assess axonal regeneration, the neurofilament-positive (NF$^+$) area at various distances from the lesion center was quantified as a percentage of the total area of axons present 1000 μm proximal. The primary antibodies included rabbit anti-METTL3 (1:500; catalog #ab195352, Abcam), mouse anti-NeuN (1:500; catalog #ab104224, Abcam), mouse anti-GFAP (1:500; catalog #GB12090, Servicebio), rabbit anti-CD68 (1:500; catalog #28058-1-AP, Proteintech), rabbit anti-Ki67 (1:500; catalog #GB111499, Servicebio), rabbit anti-chondroitin sulfate proteoglycan 4 (CSPG4; 1:500; catalog #55027-1-AP, Proteintech), rabbit anti-NF (1:500; catalog #GB12144, Servicebio), and rabbit anti-Flag (1:500; catalog #80010-1-RR, Proteintech).

For cultured cell staining, the cells were fixed in 4% paraformaldehyde for 15 min and permeabilized with 0.3% Triton X-100 at room temperature for 15 min. Subsequently, they were washed with PBS, blocked with 5% BSA, and incubated with primary antibodies overnight at 4°C and the previously mentioned secondary antibodies at room temperature for 1 h. Cells were visualized by DAPI staining. The images were acquired under a fluorescent microscope (Thunder DMi8, Leica) or a two-photon microscope (LSM 880 NLO, Zeiss), and analyzed with ImageJ software. The primary antibodies included rabbit anti-METTL3 (1:500; catalog #ab195352, Abcam), mouse anti-Myc (1:1000; catalog #2276S, Cell Signaling Technology), mouse anti-GFAP (1:500; catalog #GB12090, Servicebio), mouse anti-NeuN (1:500; catalog #ab104224, Abcam).

Nissl staining

Spinal cord tissue sections were prepared as previously described. For Nissl staining, the sections were fixed with 4% paraformaldehyde for 10 min and then incubated with cresyl violet (Beyotime) for 3 min at room temperature. Subsequently, sections were washed twice with ddH_2O followed by 95% ethanol. The sections were then dehydrated in 100% ethanol, cleared in xylene, and covered by neutral resins. The images were acquired under a microscope (Olympus), and the number of neurons was counted in ImageJ software with particles analysis module after threshold modification and cells separation, as we mentioned above.

Data analysis of gene expression omnibus databases

The spinal cord sequence profiles (GSE5296 and GSE42828) were downloaded from the Gene Expression Omnibus database. Following normalization, $\log_2$ transformation, and probe annotation in R studio software, the set of m^{6}A-related and deubiquitination-related genes and proliferative YAP1 target genes were included in a heat map plot. Pearson's correlation analyses of YAP1 and m^{6}A-related genes were preformed based on their $\log_2$-transformed expressions.

Cell lines and primary astrocyte culture

Primary astrocytes were cultured as described previously (W. Liu et al., 2021). In brief, the mouse brain was removed and cut into 0.5–1 mm^3 pieces and then incubated in 0.125% trypsin (Invitrogen) with gentle shaking at 37°C for 20 min. Following centrifugation, the tissue pellets were resuspended in DMEM and filtrated through a 100 μm nylon mesh. The single-cell suspension was cultured in poly-L-lysine precoated-T75 flasks with DMEM medium containing 10% FBS and 1% penicillin-streptomycin. Other glial cells were eliminated by shaking at 180 rpm for 30 min and 240 rpm for another 6 h when astrocytes reached a confluent state.

The HEK 293T cell line was obtained from the Cell Bank of the Chinese Academy of Science (Shanghai) and cultured in DMEM containing 10% FBS and 1% penicillin-streptomycin at 37°C with 5% CO_2.

In vitro astrocyte scratch injury assay

Astrocytes were seeded in six-well plates and allowed to reach confluence. To simulate *in vitro* behavior of astrocytes in response to spinal cord injury *in vivo*, one (for immunofluorescence staining) or several (for RNA and protein extraction) scratches were made by a sterile 200 μl pipette tip as previously reported (Li et al., 2014; Pappalardo et al., 2014). The cells were then washed three times with PBS to remove debris and cultured with DMEM medium for 48 h. The astrocytes were visualized by immunofluorescence staining of GFAP as previously described, and mitotic cells were marked by the EdU assay (Beyotime) according to the protocol from the manufacturer. Individual images (six to seven per scratch wound) were obtained and analyzed with ImageJ software as previously described (Li et al., 2014). Migration of astrocytes into the cell-free area created by scratching was quantified by measuring the area immediately after injury and 48 h after injury, and astrocytic proliferation was quantified as the proportion of EdU$^+$ astrocytes relative to all astrocytes in the entire field. The astrocytic protrusion was evaluated by measuring the lengths of migrating-cell processes (visualized with GFAP staining) surrounding the scratch wound after setting scale.

The shRNA and plasmid construction

The shRNA-control, shRNA-METTL3, shIGF2BP2, shUSP1, and shUAF1 were constructed by Genebay Biotech. The control plasmid, Flag-tagged METTL3 expression plasmid, Flag-tagged METTL3 domain plasmid, HA-tagged ubiquitin (including WT, K48 mutant, and K63 mutant) expression plasmid, IGF2BP2 expression plasmid, Myc-tagged USP1 (either WT or C90S mutant) expression plasmid, and Myc-tagged UAF1 expression plasmid were all constructed by Genebay Biotech. Primary astrocytes and HEK 293T cells were transfected using Lipofectamine 3000 reagent (Thermo Fisher Scientific) according to instructions from the manufacturer.

RNA sequencing and analysis

All gene expression changes in normal astrocytes and scratch-injured astrocytes were determined using RNA sequence analysis, which was performed by Genminix Information. Briefly, total RNA was isolated and quality RNA samples were converted into cDNA libraries. The purified products were amplified with 12–15 cycles of PCR to create the final cDNA library. Libraries were then sequenced on the Illumina HiSeq X Ten following protocols from the manufacturer. Data analysis was performed with R studio software as previously described.

Dot blot and m^{6}A quantification

Total RNA was isolated by TRIzol reagent following the protocol from the manufacturer, and polyadenylated mRNA was prepared using a GenElute mRNA Miniprep Kit (Sigma-Aldrich). Purified mRNA was then loaded onto a nylon membrane and UV cross-linked to the membrane. Following blocking with 5% BSA for 1 h, the membranes were incubated with anti-m^{6}A primary antibodies (ABclonal) at 4°C overnight and HRP-conjugated secondary antibodies for 2 h at room temperature. The membranes were visualized by an ECL detection system (Millipore). Methylene blue (catalog #319112, Sigma-Aldrich) staining was used as the loading control. The global m^{6}A level was evaluated by using an m^{6}A RNA Methylation Assay Kit (catalog #ab185912, Abcam), polyadenylated mRNA was prepared as described above, and 200 ng mRNA was used per well following instructions from the manufacturer. In brief, following sample preparation and mRNA binding, the diluted capture antibody (primary m^{6}A antibody for m^{6}A RNA capture) and detection antibody (secondary antibody for capture antibody binding) solutions were added to test wells. The m^{6}A levels were then quantified calorimetrically, based on absorbance at 450 nm.

Liquid chromatography with tandem mass spectrometry quantification of m^{6}A in mRNA

RNA m^{6}A evaluation by liquid chromatography with tandem mass spectrometry (LC-MS/MS) was performed as described previously (Xu et al., 2021). In brief, 200 ng mRNA was first incubated with nuclease P1 (Sigma-Aldrich) in 20 µl reaction buffer plus 25 mM NaCl and 2.5 mM $ZnCl_2$ at 37°C for 2 h. Then the buffer was added with 2.2 µl 1 M NH_4HCO_3 and alkaline phosphatase (Sigma-Aldrich) and incubated at 37°C for another 2 h. Samples were then subjected to centrifugation at 13,000 rpm for 10 min, and 10 µl of the solution was injected into the LC-MS/MS device. Nucleosides were quantified by retention time and ion mass transitions of 268–136 (A) and 282–150 (m^{6}A). The ratio of m^{6}A to A was calculated by standard curves.

Methylated RNA immunoprecipitation qPCR and methylated RNA immunoprecipitation sequencing

Methylated RNA immunoprecipitation (MeRIP) sequencing (MeRIP-seq) was performed and analyzed by Nanjing Jiangbei New Area Biopharmaceutical Public Service Platform. Briefly, total RNA was prepared and fragmented into 100−200 nt. The RNA was then purified using a Zymo RNA Clean and Concentrator-5 kit. Following incubation with m^{6}A-antibody-bound protein A/G magnetic beads at 4°C overnight, fragmented RNA was extracted from dynabeads and eluted using a low salt reaction buffer and high salt reaction buffer. Both the input sample and m^{6}A-IP sample were used for library construction by the NEBNext Ultra II Directional RNA Library Prep Kit (New England BioLabs) and the quality was examined by BiOptic Qsep100 Analyzer. Library sequencing was finally performed on an Illumina NovaSeq 6000 instrument with 150 bp paired-end reads. Data analyses including gene ontology and Kyoto Encyclopedia of Genes and Genomes (KEGG) enrichment were performed with R studio software, and m^{6}A enriched regions were visualized by Integrative Genomics Viewer software. For MeRIP qPCR, RT-qPCR was performed following m^{6}A-IP to evaluate the methylation level of a target mRNA. In brief, extracted RNA was treated with DNase (Thermo Fisher Scientific) to avoid DNA contaminations and then fragmented into 100−200 nt. The fragmented RNA was subsequently incubated with m^{6}A antibody for immunoprecipitation according to the protocol of the Magna MeRIP m^{6}A Kit (Millipore) followed by RT-qPCR.

RT-qPCR

Total RNA was extracted from the spinal cord or astrocytes using TRIzol reagent. The RNA was reverse transcribed into cDNA using a PrimeScript RT Reagent Kit, and RT-qPCR was subsequently performed by TB Green® Premix Ex Taq™ kit. Relative expression levels of target genes were normalized to GAPDH and quantified using the $2^{-\Delta\Delta CT}$ method. The primer sequences used are as follows: *METTL3* primer, forward 5′-CGTAGTGATAGTCCCGTGCC-3′ and reverse 5′-TGGCGTAGAGATGGCAAGAC-3′; *YAP1* primer, forward 5′-CCC TCGTTTTGCCATGAACC-3′ and reverse 5′-GCTGTATTTGCTGCT GCTGG-3′; *IGF2BP2* primer, forward 5′-ATTTCGGCCCATTCC CACAT-3′ and reverse 5′-GGCCTTCTGCTGGAGCAAT-3′; *USP1* primer, forward 5′-GGGAATCCCAGCCATTGGAA-3′ and reverse 5′-GGGTTGCTTAGTGGATGGCT-3′; *UAF1* primer, forward 5′-GGC GGAGGAAAGTGCAGGT-3′ and reverse 5′-TGTACGGATCTTGCT TGTGCT-3′; *GAPDH* primer, forward 5′-GGAGAGTGTTTCCTC GTCCC-3′ and reverse 5′-ATGAAGGGGTCGTTGATGGC-3′.

RNA degradation assay

To examine the half-life of target mRNA, actinomycin D (5 µg/ml; catalog SBR00013, Sigma-Aldrich) was added for different time periods to inhibit transcription. Total RNA was then extracted and RT-qPCR was conducted as described above.

Dual-luciferase assay

The dual-luciferase reporter assay system (Promega) was used to determine the m^{6}A modification within the 3′-UTR region of *YAP1* transcripts following instructions from the manufacturer. In brief, WT or m^{6}A-mutated (adenosine replaced by cytosine) *YAP1*-3′-UTR vectors fused with firefly luciferase and Renilla luciferase (Genebay Biotech) were cotransfected with shMETTL3 or corresponding control shRNA into primary astrocytes using Lipofectamine 3000 reagent. Cells were lysed 48 h after transfection, and firefly luciferase activity was examined to evaluate effects of m^{6}A modification on *YAP1* expression. Renilla luciferase was used to normalize the transfection efficiency of reporter plasmid.

Western blot analysis

The protein of cells or a total length of 4 mm spinal cord tissues centered on the lesion site was isolated using RIPA lysis buffer (KeyGEN BioTECH), and nucleoprotein was extracted by a nuclear protein extraction kit (Beyotime) following instructions from the manufacturer. Following denaturation at 100°C for 10 min and separation in SDS-PAGE gels, proteins were transferred to PVDF membranes. The membranes were then blocked with 5% BSA at room temperature for 2 h and incubated with primary antibodies at 4°C overnight, and HRP-conjugated secondary antibodies (1:5000; Jackson ImmunoResearch) at room temperature for 2 h. Finally, protein bands were detected using ECL reagent (Beyotime) and quantified by ImageJ software. The primary antibodies included rabbit anti-METTL3 (1:1000; catalog #1073-1-AP, Proteintech), rabbit anti-Ub (1:1000; catalog #10201-1-AP, Proteintech), rabbit anti-USP1 (1:1000; catalog #A6785, ABclonal Technology), rabbit anti-UAF1 (1:1000; catalog #16503-1-AP, Proteintech), rabbit anti-Flag (1:1000; catalog #80010-1-RR, Proteintech), mouse anti-Myc (1:1000; catalog #2276S, Cell Signaling Technology), rabbit anti-HA (1:1000; catalog #51064-2-AP, Proteintech), mouse anti-GFAP (1:1000; catalog #GB12090, Servicebio), rabbit anti-YAP1 (1:1000; catalog #13584-1-AP, Proteintech), rabbit anti-Histone H3 (1:1000; catalog #GB11102, Servicebio), rabbit anti-IGF2BP2 (1:1000; catalog #11601-1-AP, Proteintech), and mouse anti-GAPDH (1:1000; catalog #60004-1-Ig, Proteintech).

Immunoprecipitation

Protein of cells or tissues was extracted as described above and precleared using appropriate control IgG together with 20 µl protein A/G plus-agarose (Santa Cruz Biotechnology) and incubated at 4°C for 30 min. Following centrifugation, the lysate was immunoprecipitated with indicated primary antibodies at 4°C for 1 h, and 20 µl protein A/G plus-agarose was added for incubation overnight. Immunocomplexes were collected and washed five times with lysis buffer. The bound protein was then subjected to SDS-PAGE for immunoblotting.

For silver staining and IP-MS, cellular extracts of primary astrocytes expressing vector of Flag-METTL3 were prepared and subsequently subjected to BeyoMag anti-Flag magnetic beads (Beyotime) and eluted by 3X Flag peptides (Beyotime) to remove IgG heavy and light chains. The eluates were then separated with SDS-PAGE for mass spectrometry (Thermo Fisher Scientific) and silver staining (Beyotime) following instructions from the manufacturer.

Molecular docking

Molecular docking assay was performed to investigate the interaction mode between USP1/UAF1 complex and METTL3 using Discovery Studio

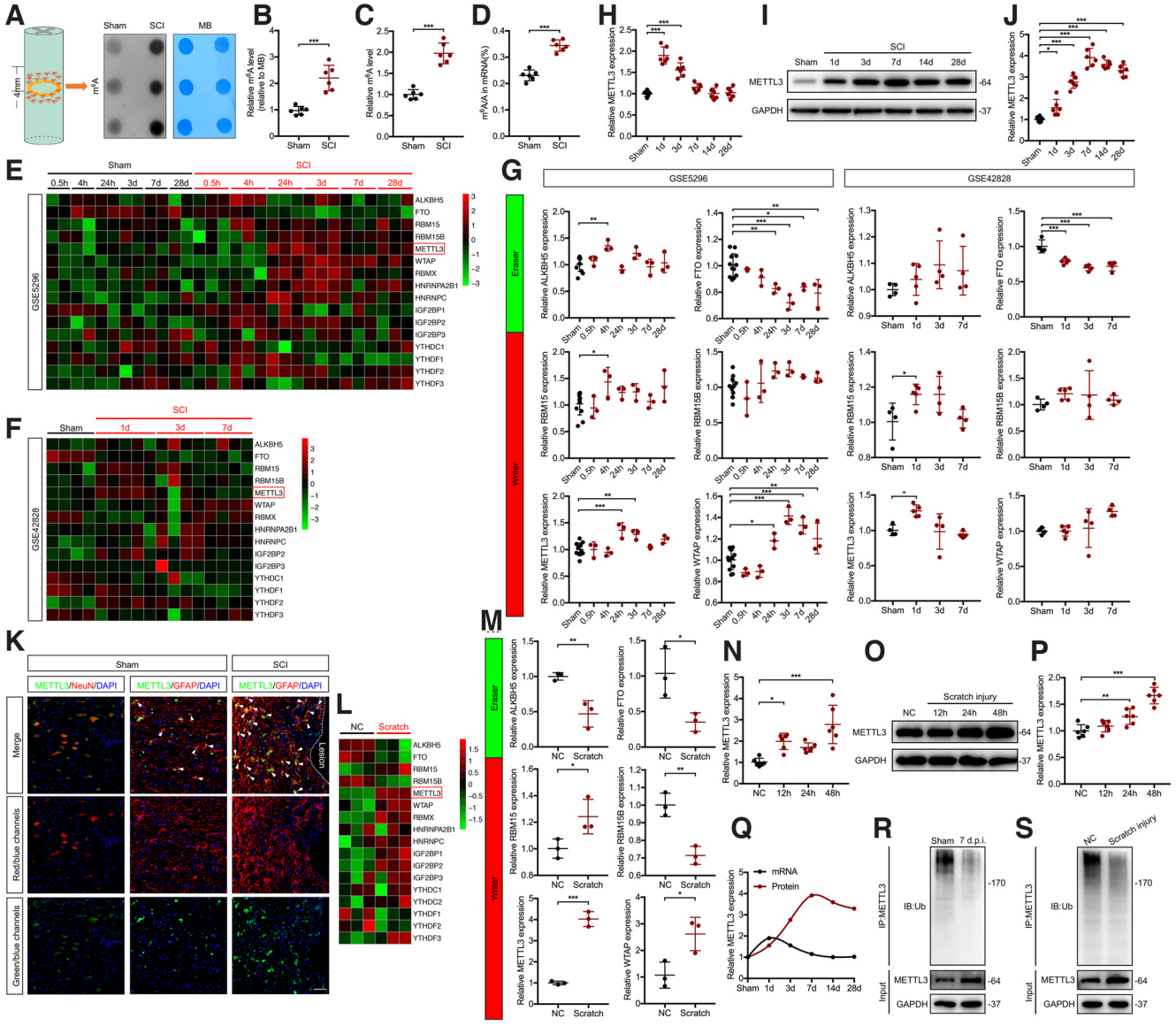

Figure 1. RNA m^{6}A methylation and astrocytic METTL3 level are upregulated after SCI. ***A***, ***B***, Representative images and quantification of m^{6}A dot blot in 4 mm sham and injured spinal cord. MB, Methylene blue staining (as a loading control); ***$p < 0.001$. ***C***, Global m^{6}A level was detected by colorimetric m^{6}A quantification assay; ***$p < 0.001$. ***D***, LC-MS/MS quantification of m^{6}A/A ratio in sham and SCI groups; ***$p < 0.001$. ***E***, Heat map of a set of m^{6}A-related genes in GSE5296. ***F***, Heat map of a set of m^{6}A-related genes in GSE42828. ***G***, Expression of writers and erasers in GSE5296 and GSE42828; *$p < 0.05$, **$p < 0.01$, ***$p < 0.001$. ***H***, Relative *METTL3* mRNA level of spinal cord at indicated time after SCI was evaluated by RT-qPCR; ***$p < 0.001$. ***I***, ***J***, Relative METTL3 protein level of spinal cord at indicated time after SCI was evaluated and quantified; *$p = 0.0188$, ***$p < 0.001$. ***K***, Immunofluorescence costaining of METTL3 with NeuN or GFAP in mice spinal cord uninjured or 7 d postinjury (arrows indicate METTL3$^+$/GFAP$^+$ cells). Scale bar, 100 μm. ***L***, Heat map of a set of m^{6}A-related genes in scratch-injured astrocytes compared with the corresponding control. ***M***, Expression of writers and erasers in scratch-injured astrocytes; *$p < 0.05$, **$p < 0.01$, ***$p < 0.001$. ***N***, Relative *METTL3* mRNA level of primary astrocytes at the indicated time after scratch injury was evaluated by RT-qPCR; *$p = 0.0104$, ***$p < 0.001$. ***O***, ***P***, Relative METTL3 protein level and quantification of primary astrocytes at indicated time after scratch injury was evaluated; **$p = 0.0063$, ***$p < 0.001$. ***Q***, Temporal expression of spinal cord METTL3 mRNA and protein level at the indicated time following SCI. ***R***, Ubiquitination levels of endogenous METTL3 protein in spinal cord with or without injury. ***S***, Ubiquitination levels of endogenous METTL3 protein in primary astrocytes with or without scratch injury. One-way ANOVA followed by *post hoc* Bonferroni correction (***G***, ***H***, ***J***, ***N***, ***P***); Student's two-tailed unpaired *t* test (***B***, ***C***, ***D***, ***M***). Data of RNA sequence comparing scratch-injured and uninjured astrocytes are shown in Extended Data Figure 1-1.

software (BIOVIA). The three-dimensional structures of USP1/UAF1 and METTL3 were downloaded from the Research Collaboratory for Structural Bioinformatics Protein Data Bank database. In brief, after removing crystallographic water molecules, the Prepare Protein module was used to remove the polyconformation of the target protein and supplement the incomplete amino acid residues. The Prepare Ligands module was then used to obtain an effective three-dimensional conformation. Following binding site definition, molecular docking was performed with the LibDock module.

Statistical analysis

All data are shown as mean ± SD, and statistical analysis was performed in GraphPad Prism (version 8.0) software. Student's *t* test was used for comparisons between two groups, and one-way or two-way ANOVA followed by the *post hoc* Bonferroni correction was used for multivariate analysis. A p value < 0.05 was considered to be significant.

Results

RNA m^{6}A methylation and astrocytic METTL3 level are upregulated after SCI

The RNA m^{6}A methylation level of the spinal cord was detected 7 d after SCI. The m^{6}A dot blot (Fig. 1*A*,*B*), colorimetric m^{6}A quantification assay (Fig. 1*C*), and LC-MS/MS analysis (Fig. 1*D*) demonstrated the global hypermethylation of m^{6}A in

polyadenylated RNA after SCI. To elucidate this phenomenon, two comprehensive databases of temporal changes in gene expression after SCI (GSE5296 and GSE42828) were analyzed, and a set of m^{6}A-related genes, including writers, erasers, and readers, was compiled. The GSE5296 database demonstrated that writers were significantly upregulated after SCI, including *RBM15* (0.4 h after SCI), *METTL3* (days 1 and 3 postinjury), and *WTAP* (days 1, 3, 7, and 28 postinjury). In GSE42828, both *RBM15* and *METTL3* were remarkably enhanced 1 d after SCI, whereas the eraser *FTO* was decreased in both databases (Fig. 1*E–G*).

Given that METTL3 is a core subunit of methyltransferase complex mainly responsible for deposition of m^{6}A into target mRNA, and other writers only play an auxiliary role (Meyer and Jaffrey, 2014; Zeng et al., 2020), we then focused on the function of METTL3 in spinal cord injury. *METTL3* mRNA level was upregulated after SCI and peaked 1 d after injury, as demonstrated by the two databases (Fig. 1*G*) and verified by RT-qPCR (Fig. 1*H*). The protein level of METTL3 was enhanced as well after SCI with a peak at day 7 postinjury (Fig. 1*I,J*). To further investigate the cellular location of METTL3, immunofluorescence staining of mice spinal cords was performed. The result showed that METTL3 was mainly located in neurons with minor expression in inactive astrocytes, which was consistent with previous studies (Chen et al., 2019; Zhang et al., 2020). However, reactive astrocytes adjacent to the epicenter showed an augmented expression of METTL3 compared with inactivated astrocytes (Fig. 1*K*). To validate whether astrocytic METTL3 was upregulated after SCI, an *in vitro* astrocyte scratch injury assay was then conducted to simulate reactive astrogliosis *in vivo* followed by RNA sequencing (RNA-seq) analysis (Extended Data Fig. 1-1). Following the scratch, levels of m^{6}A writers in astrocytes were strikingly augmented, whereas erasers were attenuated (Fig. 1*L,M*). Experimentally, a noticeable increase in the level of astrocytic METTL3 was observed after scratch injury (Fig. 1*N–P*).

Of interest, when comparing the temporal expression of METTL3 mRNA and protein after SCI, we noted that even if the mRNA level returned to baseline after 7 d, its protein expression still maintained a high level until 28 d after SCI (Fig. 1*Q*). Obviously, an increase of mRNA level alone could not explain this phenomenon, so something else might regulate METTL3 protein expression, especially in the mid and late stages of SCI. One possibility is that there exists a post-translational modification regulating METTL3 protein expression. Given that ubiquitination of METTL3 was previously reported (Sun et al., 2020), we speculated that deubiquitination modification might contribute to the high level of METTL3 protein after SCI. Indeed, the ubiquitin level of endogenous METTL3 at 7 d after SCI was attenuated (Fig. 1*R*), and a parallel result was observed in primary astrocytes subjected to scratch injury *in vitro* (Fig. 1*S*), suggesting that deubiquitination modification was responsible for the high level of METTL3 after SCI. Together, m^{6}A methylation and astrocytic METTL3 level are upregulated after SCI, and there exists a deubiquitination modification that modulates METTL3 protein expression.

USP1/UAF1 complex interacts with METTL3

To further investigate METTL3-interacting deubiquitinases, mass spectrometry was conducted on a coimmunoprecipitated Flag-METTL3 complex from primary astrocytes (Fig. 2*A*), and USP1 along with its stoichiometric partner UAF1 were identified as potential substrates precipitated by METTL3 (Fig. 2*B*). In parallel, we found that *USP1* expression was significantly enhanced after SCI (Fig. 2*C,D,F,G*), as well as in scratch-injured astrocytes (Fig. 2*E,H*), which might account for prolonged upregulation of METTL3. However, there was no increase in level of *UAF1* after SCI both *in vivo* and *in vitro* (Fig. 2*I–K*). Results of RT-qPCR and Western blot analysis further verified above results *in vitro* and *in vivo* (Fig. 2*L–Q*). Moreover, a coimmunoprecipitation (Co-IP) assay validated that both endogenous USP1 and UAF1 could be coprecipitated by endogenous METTL3 (Fig. 2*R*), and *in vitro* scratch injury induced more USP1 and UAF1 coprecipitated by METTL3 (Fig. 2*S*). A reverse Co-IP assay further confirmed the interaction between endogenous USP1/UAF1 complex and METTL3 (Fig. 2*T*). To investigate the combination of exogenous METTL3 and USP1/UAF1 complex, we expressed Flag-METTL3 and Myc-USP1 or Myc-UAF1 in HEK 293T cells. As expected, Flag-tagged METTL3 could also coprecipitate with Myc-tagged USP1 or UAF1 (Fig. 2*U,V*). Costaining of METTL3 with Myc-tagged USP1 or UAF1 in primary astrocytes directly revealed the colocation of METTL3 with USP1/UAF1 complex in the nucleus (Fig. 2*W*). Computer molecular docking further indicated an interaction between METTL3 and the USP1/UAF1 complex (Fig. 2*X*).

Full-length METTL3 contains 580 amino acids and is composed of a zinc finger domain and a methyltransferase domain (also known as the MTase domain). Traditionally, the MTase domain was recognized to be responsible for RNA methylation modification following recognition and capture of target mRNA by its zinc finger domain (Śledź and Jinek, 2016; Huang et al., 2019). To identify the METTL3 domain responsible for binding to the USP1/UAF1 complex, we next constructed a series of Flag-tagged METTL3 truncated mutants based on its structure (Fig. 2*Y*) and transfected them into HEK 293T cells. Co-IP results demonstrated that the full-length METTL3 and M3 truncated mutant coprecipitated with Myc-tagged USP1 and UAF1, whereas M1 and M2 truncated mutants lost the ability to bind to USP1 and UAF1 (Fig. 2*Z*), which indicated that the methyltransferase domain of METTL3 plays an essential role in protein binding as well. Collectively, these data indicate that the USP1/UAF1 complex interacts with METTL3 via specifically binding to its MTase domain.

The USP1/UAF1 complex deubiquitinates and stabilizes METTL3

Because METTL3 interacts with the USP1/UAF1 complex, we then characterized the regulation of METTL3 by USP1 and UAF1. As shown in Figure 3*A*, the METTL3 level was enhanced by overexpression of USP1 or UAF1, which was more obvious when both USP1 and UAF1 were overexpressed. However, addition of ML323 (USP1/UAF1 complex specific inhibitor; catalog #HY-17543, MedChem Express) could significantly abolish this effect via attenuating USP1/UAF1 expression. Moreover, knockdown of USP1 or UAF1 attenuated METTL3 expression, and the combined ablation of the USP1/UAF1 complex showed a stronger METTL3 suppressive effect (Fig. 3*B*). Of note, addition of proteasome inhibitor MG132 (catalog #HY-13259, MedChem Express) could reverse the decline of astrocytic METTL3 following depletion of USP1 or UAF1 (Fig. 3*C,D*). Additionally, after inhibiting the astrocyte protein translation with 10 μg/ml cycloheximide (CHX; catalog #HY-12320, MedChem Express), we found that the silencing of USP1 and UAF1 significantly shortened the half-life of the METTL3 protein, and USP1/UAF1 double knockdown achieved a stronger suppression of METTL3 level (Fig. 3*E*).

It is well known that deubiquitination is a post-translational modification that selectively hydrolyzes linear ubiquitin chains from target proteins to inhibit its ubiquitin-proteasomal

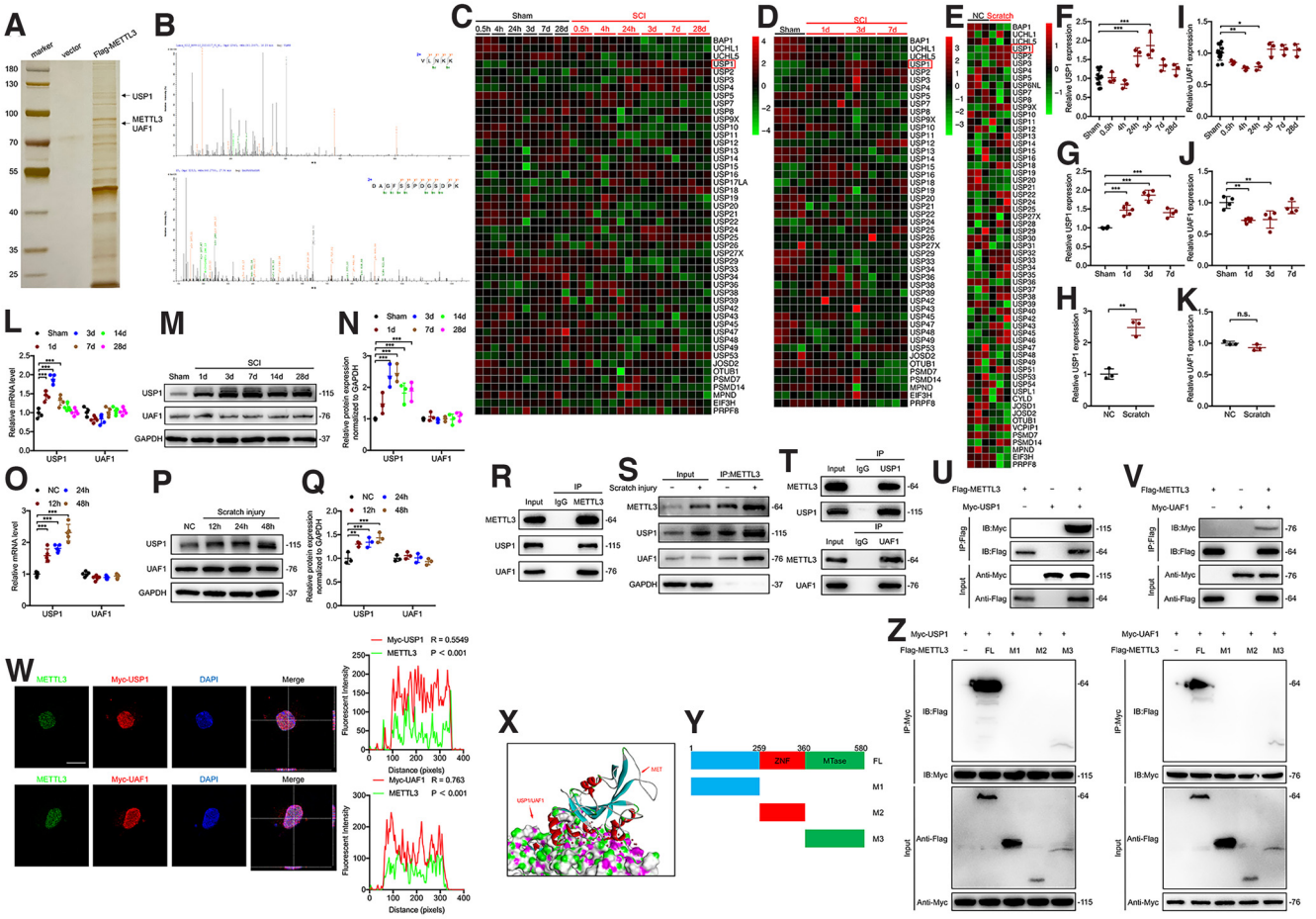

Figure 2. USP1/UAF1 complex interacts with METTL3. ***A***, Silver-stained gel of astrocytic proteins coimmunoprecipitated using anti-Flag magnetic beads and eluted by Flag peptides. ***B***, Mass spectrometry identified specific peptides of USP1 (top) and UAF1 (bottom) in immunoprecipitated METTL3 complexes. ***C–E***, Heat maps of a set of deubiquitinating enzymes in GSE5296 (***C***), GSE42828 (***D***), and scratch injured astrocytes (***E***). ***F–H***, Relative *USP1* expression in GSE5296 (***F***), GSE42828 (***G***), and RNA sequence of scratch injured astrocytes (***H***); $^{**}p = 0.0011$, $^{***}p < 0.001$. ***I–K***, Relative *UAF1* expression in GSE5296 (***I***), GSE42828 (***J***), and RNA sequence of scratch-injured astrocytes (***K***); $^{*}p = 0.0127$, $^{**}p < 0.01$. ***L***, Relative mRNA expression of *USP1 and UAF1* at the indicated times after SCI was examined by RT-qPCR; $^{***}p < 0.001$. ***M***, ***N***, Relative protein expression of USP1 and UAF1 at the indicated times after SCI were examined and quantified; $^{***}p < 0.001$. ***O***, Relative mRNA expression of astrocytic *USP1 and UAF1* at the indicated times after scratch injury was examined by RT-qPCR; $^{***}p < 0.001$. ***P***, ***Q***, Relative protein expression of astrocytic USP1 and UAF1 at the indicated times after scratch injury was examined and quantified; $^{**}p = 0.0025$, $^{***}p < 0.001$. ***R***, Protein extracts from primary astrocytes were subjected to immunoprecipitation with anti-METTL3 or anti-IgG and then immunoblotted with indicated antibodies. ***S***, At 48 h after scratch injury, equal amounts of astrocytic protein lysates were immunoprecipitated using anti-METTL3 and examined by immunoblotting with indicated antibodies. ***T***, Protein lysate of primary astrocytes was immunoprecipitated with anti-USP1 or anti-UAF1 and then evaluated by immunoblotting with anti-METTL3. ***U***, ***V***, Extracts from HEK 293T cells transfected with Flag-METTL3 and Myc-USP1 (***U***) or Myc-UAF1 (***V***) were immunoprecipitated with anti-Flag, followed by immunoblotting with anti-Myc and anti-Flag. ***W***, Primary astrocytes transfected with Myc-USP1 or Myc-UAF1 were immunofluorescence stained using anti-METTL3 and anti-Myc. Scale bar, 10 μm. Correlation was analyzed using ImageJ software. ***X***, Molecular dock of METTL3 and USP1/UAF1 complex. ***Y***, Schematic diagram of Flag-tagged full-length METTL3 and corresponding truncated mutants. ***Z***, HEK 293T cells were transfected with Myc-USP1 (left) or Myc-UAF1 (right) along with Flag-tagged METTL3 or its mutants. Cell lysates were immunoprecipitated with anti-Myc, followed by immunoblotting with indicated antibodies. One-way ANOVA followed by *post hoc* Bonferroni correction (***F***, ***G***, ***I***, ***J***, ***L***, ***N***, ***O***, ***Q***); Student's two-tailed unpaired *t* test (***H***, ***K***).

degradation (B. Liu et al., 2021). Based on the above results, we further investigated whether USP1/UAF1 complex could remove ubiquitination chain of METTL3 through an *in vivo* ubiquitination assay. As expected, ectopic expression of both USP1 and UAF1 considerably suppressed ubiquitination of endogenous METTL3 in primary astrocytes (Fig. 3*F*,*G*), whereas catalytically inactive mutant (C90S) of USP1 lost the ability to deubiquitinate METTL3 (Fig. 3*F*). On the other hand, depletion of USP1 and UAF1 reversely enhanced ubiquitination level of endogenous METTL3 (Fig. 3*H*). To further confirm the deubiquitination effect of USP1/UAF1 complex on METTL3, Flag-tagged METTL3, Myc-tagged USP1 (either WT or C90S mutant), Myc-tagged UAF1, and HA-tagged Ub were expressed in HEK 293T cells. Similar to the above results, overexpression of WT USP1 and UAF1 removed ubiquitination of METTL3 (Fig. 3*I*,*J*), whereas the C90S mutant abolished this effect (Fig. 3*I*). Furthermore, depletion of USP1 and UAF1 significantly augmented ubiquitination of METTL3 in HEK 293T cells, and double knockdown led to increased ubiquitination (Fig. 3*K*). It is well known that there are two major polyubiquitination chains named the K48-linkage and K63-linkage. K48-linkage is a canonical signal for proteasomal degradation, whereas K63-linked polyubiquitin is responsible for nonproteasomal pathways, including intracellular signaling, DNA repair, and the endocytosis process (Grice and Nathan, 2016). To identify which polyubiquitination of METTL3 was influenced by the USP1/UAF1 complex, we expressed HA-K48-Ub or HA-K63-Ub in HEK 293T cells and repeated the *in vivo* ubiquitination assay. Both USP1 and UAF1 considerably inhibited METTL3 polyubiquitination with K48-linkage, but not

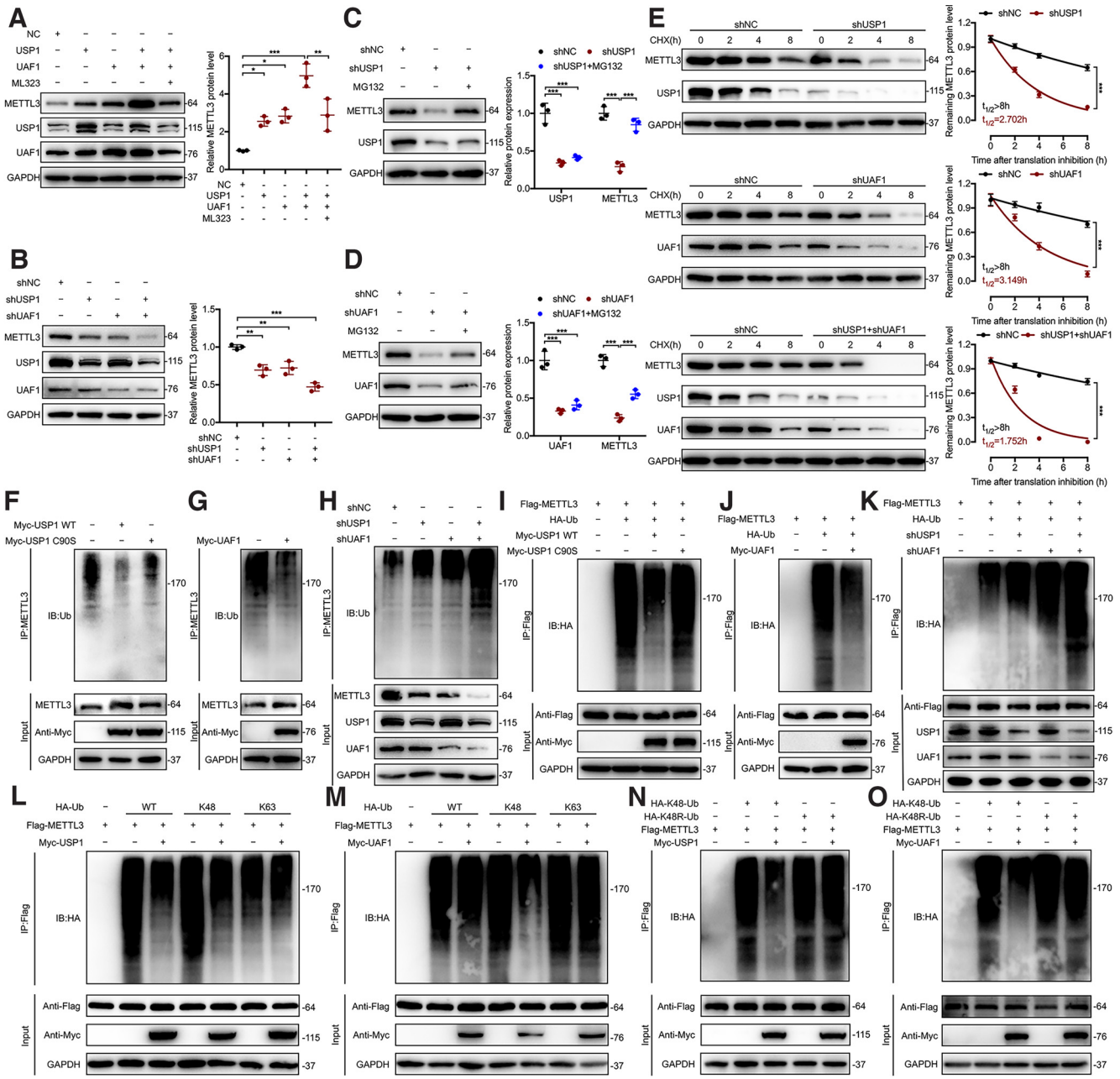

Figure 3. USP1/UAF1 complex deubiquitinates and stabilizes METTL3. ***A***, Expression of astrocytic METTL3 was evaluated by Western blotting following overexpression of USP1 or UAF1 with or without addition of 30 mM ML323 for 4 h; $*p < 0.05$, $**p = 0.0054$, $***p < 0.001$. ***B***. Effects of USP1 or UAF1 knockdown on astrocytic METTL3 protein expression were assessed via Western blotting; $**p < 0.01$, $***p < 0.001$. ***C***, ***D***, Analysis of astrocytic METTL3 level after USP1 (***C***) or UAF1 (***D***) depletion with or without treatment of 10 μM proteasome inhibitor MG132 for 4 h; $***p < 0.001$. ***E***, Effects of USP1 or UAF1 silencing on remaining astrocytic METTL3 level at the indicated times after translation inhibition was evaluated by Western blotting; $***p < 0.001$. ***F***, ***G***, Cell lysates of primary astrocytes transfected with Myc-USP1 and Myc-USP1 C90S mutant (***F***) or Myc-UAF1 (***G***) were immunoprecipitated with anti-METTL3, followed by immunoblotting with indicated antibodies. ***H***, Ubiquitination levels of METTL3 in astrocytes silencing USP1 or UAF1 were determined via immunoprecipitation using anti-METTL3, followed by immunoblotting with indicated antibodies. ***I***, ***J***, Proteins of HEK 293T cells transfected with Flag-METTL3, HA-Ub, Myc-USP1, Myc-USP1 C90S (***I***), and Myc-UAF1 (***J***) were subjected to immunoprecipitation using anti-Flag and then immunoblotted with indicated antibodies. ***K***, Following USP1 or UAF1 depletion, lysates from HEK 293T cells transfected with Flag-METTL3 and HA-Ub were immunoprecipitated with anti-Flag and then immunoblotted with indicated antibodies. ***L***, ***M***, Lysates from HEK 293T cells transfected with HA-Ub, HA-K48-Ub, HA-K63-Ub, Flag-METTL3, Myc-USP1 (***L***), and UAF1 (***M***), followed by immunoprecipitation with anti-Flag and subsequent immunoblotting with anti-HA. ***N***, ***O***, Coimmunoprecipitation analysis of HEK 293T cells transfected with HA-K48-Ub, HA-K48R-Ub, Flag-METTL3, Myc-USP1 (***N***), and Myc-UAF1 (***O***), followed by immunoprecipitation with anti-Flag and then immunoblotting with anti-HA. One-way ANOVA followed by *post hoc* Bonferroni correction (***A–D***); two-way ANOVA followed by *post hoc* Bonferroni correction (***E***); nonlinear regression of one phase decay (***E***).

with K63-linkage (Fig. 3*L*,*M*), and expression of K48R ubiquitin partly abolished this effect (Fig. 3*N*,*O*). Together, these data indicated that the USP1/UAF1 complex targets METTL3 and inhibits its degradation by selectively removing K48-linked ubiquitination of the METTL3 protein.

Knockdown of astrocytic METTL3 inhibits astrogliosis and wound healing *in vitro*

Based on the upregulation of astrocytic METTL3 after SCI, we intended to knock down METTL3 *in vitro* to investigate its functions in scratch-injured astrocytes. As expected, the m^{6}A level of

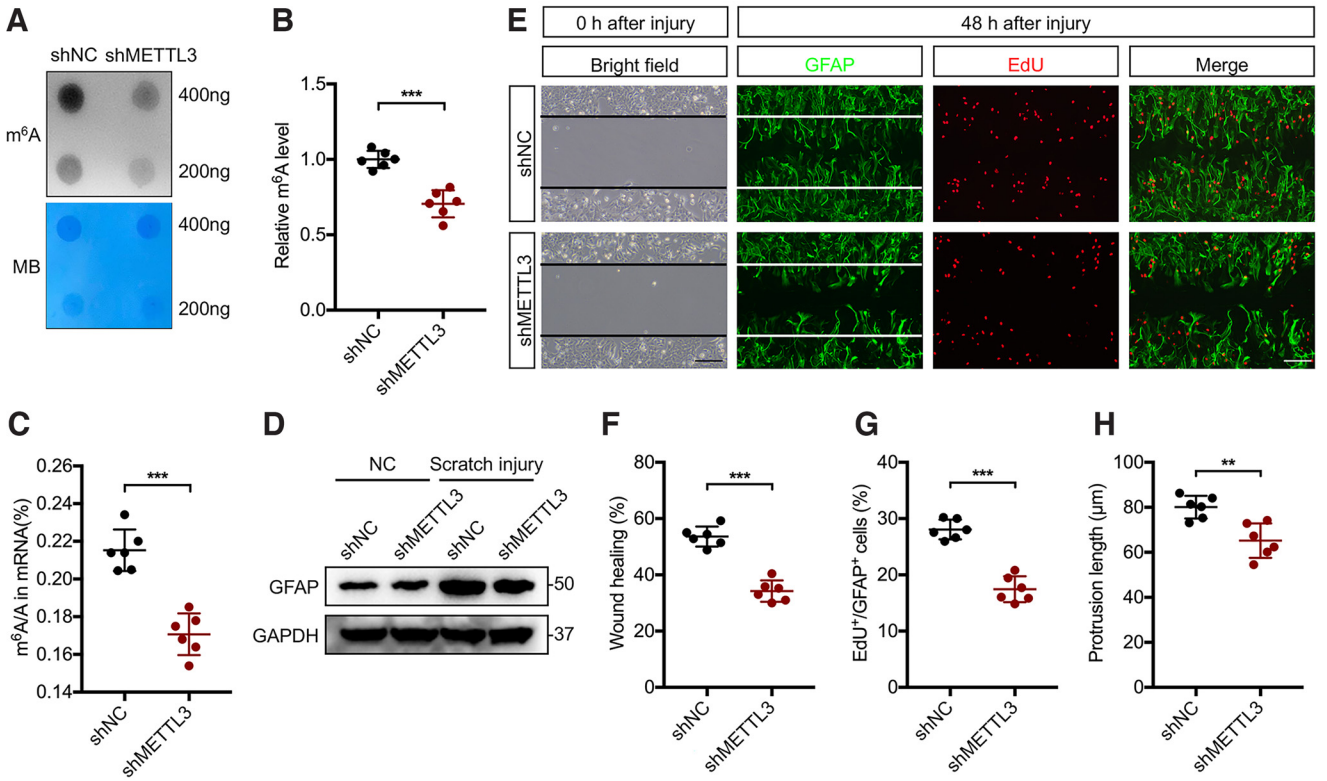

Figure 4. Knockdown of astrocytic METTL3 inhibits astrogliosis and wound healing *in vitro*. ***A–C***, The RNA methylation levels of primary astrocytes after METTL3 knockdown were evaluated using a m^{6}A dot blot (***A***), colorimetric m6A quantification assay (***B***), and LC-MS/MS analysis (***C***); ***$p < 0.001$. ***D***, GFAP protein expression of primary astrocytes transfected with shRNA-control (shNC) or shRNA-METTL3 (shMETTL3) after scratch injury. ***E***, Representative immunofluorescence images of GFAP and EdU in primary astrocytes transfected with shNC or shMETTL3 after scratch injury. ***F–H***, Quantification of wound healing ability (***F***), EdU$^+$ ratio (***G***), and protrusion length (***H***) of astrocytes transfected with shNC or shMETTL3; **$p = 0.0027$, ***$p < 0.001$. Student's two-tailed unpaired *t* test (***B***, ***C***, ***F–H***). Scale bar, 100 μm.

primary astrocytes declined following METTL3 knockdown (Fig. 4*A–C*). Furthermore, METTL3 silencing considerably suppressed the GFAP upregulation (Fig. 4*D*) and wound healing ability of injured astrocytes (Fig. 4*E*,*F*), and inhibited astrocytic proliferation as revealed by an EdU assay (Fig. 4*E*,*G*). Moreover, protrusion of astrocytes was significantly shortened following METTL3 knockdown (Fig. 4*E*,*H*). These results indicate that METTL3 might play an essential role in reactive astrogliosis.

Conditional METTL3 deletion in astrocytes hinders functional recovery and suppresses reactive astrogliosis after SCI

To assess the biological functions of astrocytic METTL3 *in vivo* after SCI, we generated mice with conditional knockout of METTL3 in astrocyte (Mettl3^{CKO}) by crossing mice with loxP sites flanking exon 2 and three of *METTL3* (Mettl3$^{fl/fl}$; Fig. 5*A*) with GFAP-Cre mice. Following genotype identification, knockout efficiencies in cerebellum, cortex, hippocampus, spinal cord, as well as cultured primary astrocytes were detected by Western blotting (Fig. 5*B–E*). Immunofluorescence staining of GFAP demonstrated that there were no remarkable changes in astrocyte size after METTL3 deletion (Fig. 5*F*,*G*). Furthermore, both Nissl staining and NeuN immunofluorescence staining of spinal cord longitudinal sections showed no pronounced differences in the number and distribution of neurons between Mettl3$^{fl/fl}$ and Mettl3^{CKO} mice (Fig. 5*H–K*). Additionally, body weight gain of Mettl3$^{fl/fl}$ and Mettl3^{CKO} mice was comparable at different developmental stages (Fig. 5*L*). In terms of functional behaviors, we noted that both Mettl3$^{fl/fl}$ and Mettl3^{CKO} mice reached nine points in the BMS score (Fig. 5*M*), and astrocytic METTL3 knockout did not influence the gait of mice, as evaluated by stride length and width (Fig. 5*N*,*O*). In sum, these results indicated that METTL3 deletion in astrocytes has no effects on spinal cord development and motor functions of mice without SCI.

Next, to evaluate the role of astrocytic METTL3 after SCI, a series of functional behavioral analyses were conducted on Mettl3$^{fl/fl}$ and Mettl3^{CKO} mice at an indicated time after injury (Fig. 6*A*). First of all, m^{6}A dot blot (Fig. 6*B*), colorimetric m^{6}A quantification assay (Fig. 6*C*), and LC-MS/MS analysis (Fig. 6*D*) validated that METTL3 deletion reduced the global mRNA m^{6}A methylation level of mouse spinal cord, and METTL3 knockout significantly suppressed the upregulation of GFAP expression after SCI, which remained unchanged before injury (Fig. 6*E*). Of note, there was a remarkable decrease of tactile sensitivity in Mettl3^{CKO} mice at 28 d postinjury compared with Mettl3$^{fl/fl}$ mice (Fig. 6*F*), and in motor function, astrocytic METTL3 deletion considerably suppressed locomotor recovery after SCI, as evaluated by the BMS score (Fig. 6*G*), footprint analysis (Fig. 6*H*), rotarod test (Fig. 6*I*), and ladder walking test (Fig. 6*J*). Furthermore, it appeared that the hindlimb nerve conduction function of Mettl3^{CKO} mice was significantly deteriorated with lower amplitude and longer latencies of MEPs compared with Mettl3$^{fl/fl}$ mice (Fig. 6*K*).

On day 14 postinjury, costaining of GFAP and CD68 demonstrated that conditional METTL3 deletion resulted in impaired reactive astrogliosis with a larger lesion area and more widespread infiltration of CD68$^+$ macrophages/microglia after SCI compared with Mettl3$^{fl/fl}$ mice (Fig. 6*L*). Additionally, the Ki67-labeled mitotic astrocytes in Mettl3^{CKO} mice were found in lower amounts than in Mettl3$^{fl/fl}$ mice after SCI (Fig. 6*M*). CSPG4, a

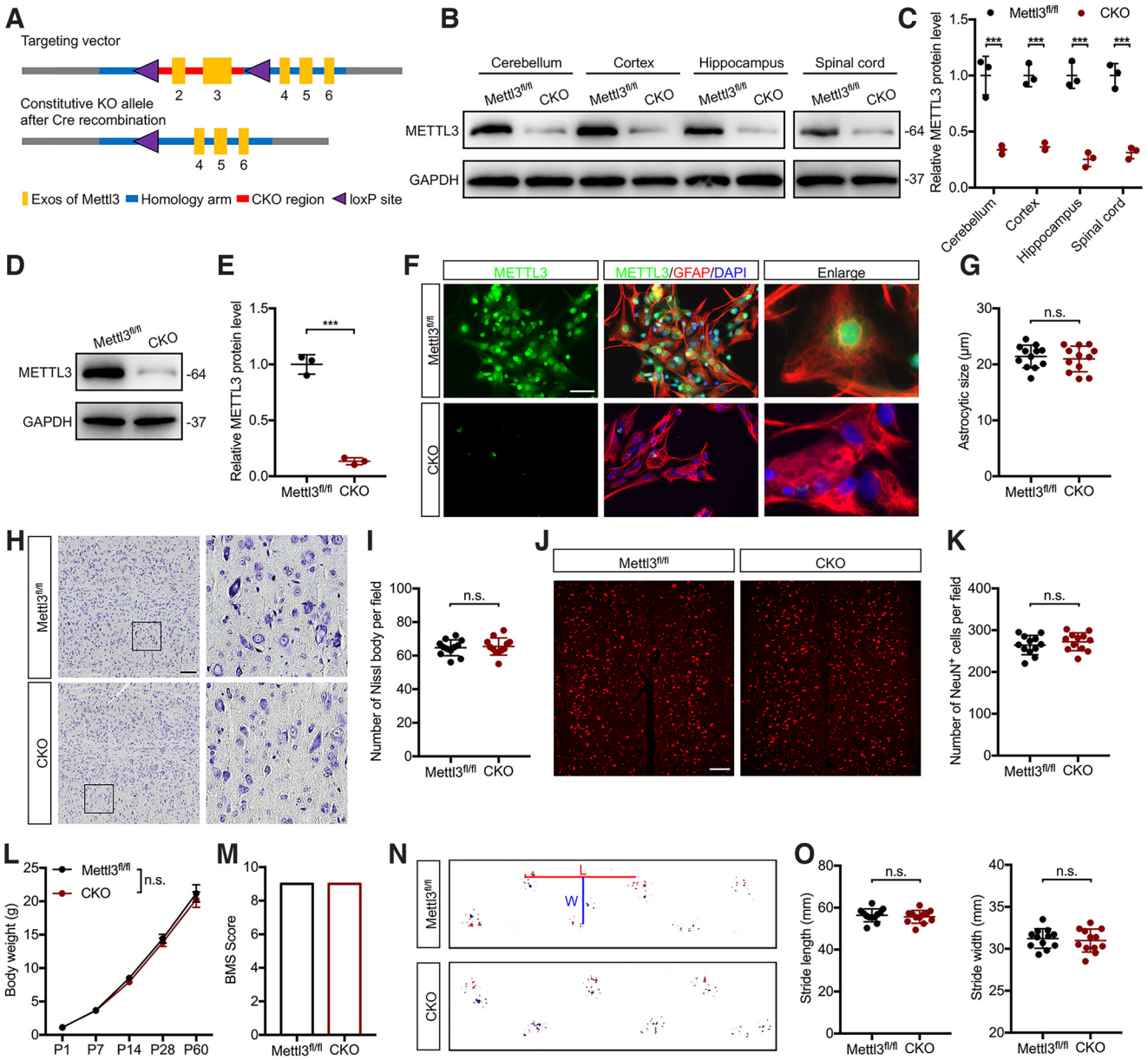

Figure 5. Conditional METTL3 deletion in astrocytes has no effects on spinal cord development and motor functions without SCI. ***A***, Schematic strategy of *METTL3*$^{fl/fl}$ mice construction. ***B–E***, Efficiency of METTL3 deletion in cerebellum, cortex, hippocampus, spinal cord, as well as cultured astrocytes were detected by Western blots; ***$p < 0.001$. ***F***, ***G***, Representative immunofluorescence images of GFAP and METTL3 in cultured astrocytes (***F***) and quantification of astrocytic sizes (***G***). Scale bar, 50 μm. ***H–K***, Nissl staining and immunofluorescence staining of neurons comparing spinal cords from Mettl3$^{fl/fl}$ mice with Mettl3^{CKO} mice and quantification of neuron number. Scale bar, 100 μm. ***L***, Body weight of Mettl3$^{fl/fl}$ mice and Mettl3^{CKO} mice at different development stages. ***M***, BMS score of Mettl3$^{fl/fl}$ and Mettl3^{CKO} mice without SCI. ***N***, ***O***, Representative images of gait from Mettl3$^{fl/fl}$ and Mettl3^{CKO} mice (***N***) and quantification of stride length and width (***O***). Student's two-tailed unpaired *t* test (***C***, ***E***, ***G***, ***I***, ***K***, ***M***, ***O***). Two-way ANOVA followed by *post hoc* Bonferroni correction (***L***).

recognized potent inhibitor of axonal growth with increased expression in both fibrotic and glial scar derived from pericytes, activated macrophages, and oligodendrocyte progenitors after SCI (Jones et al., 2002; Hesp et al., 2018), was highly expressed and widely spread by METTL3 knockout (Fig. 6*N*). We considered that METTL3 CKO might attenuate reactive astrogliosis *in vivo*, which in turn leads to spread of inflammatory cells and brings further damage to nearby tissues. To verify our speculation, staining of a neuron marker was performed to further assess survival of neurons in specific zones (Z1–Z4), located at different distances from the lesion border as previously described (Wanner et al., 2013). Indeed, a considerable decrease of neurons in the Z1–Z2 zones of Mettl3^{CKO} mice was observed, whereas the Z3–Z4 zones and uninjured regions showed no difference in Mettl3$^{fl/fl}$ mice (Fig. 6*O*). The NF is regarded as an essential element in neural network and axonal transport. We noted that METTL3 CKO significantly inhibited NF^{+} axon regeneration after SCI (Fig. 6*P*). Overall, these results suggest that METTL3 deletion remarkably inhibits reactive astrogliosis and induces widespread neuroinflammation and scar formation, thus impairing viable neurons and axonal regeneration, and eventually deteriorating motor and sensory function recovery following SCI.

YAP1 is a potential target of METTL3 in astrocytes

To explore potential targets and underlying mechanism of METTL3 in reactive astrogliosis, MeRIP-seq combined with RNA-seq (Extended Data Fig. 7-1) were performed using primary astrocytes with or without METTL3 knockdown. A total of 2328

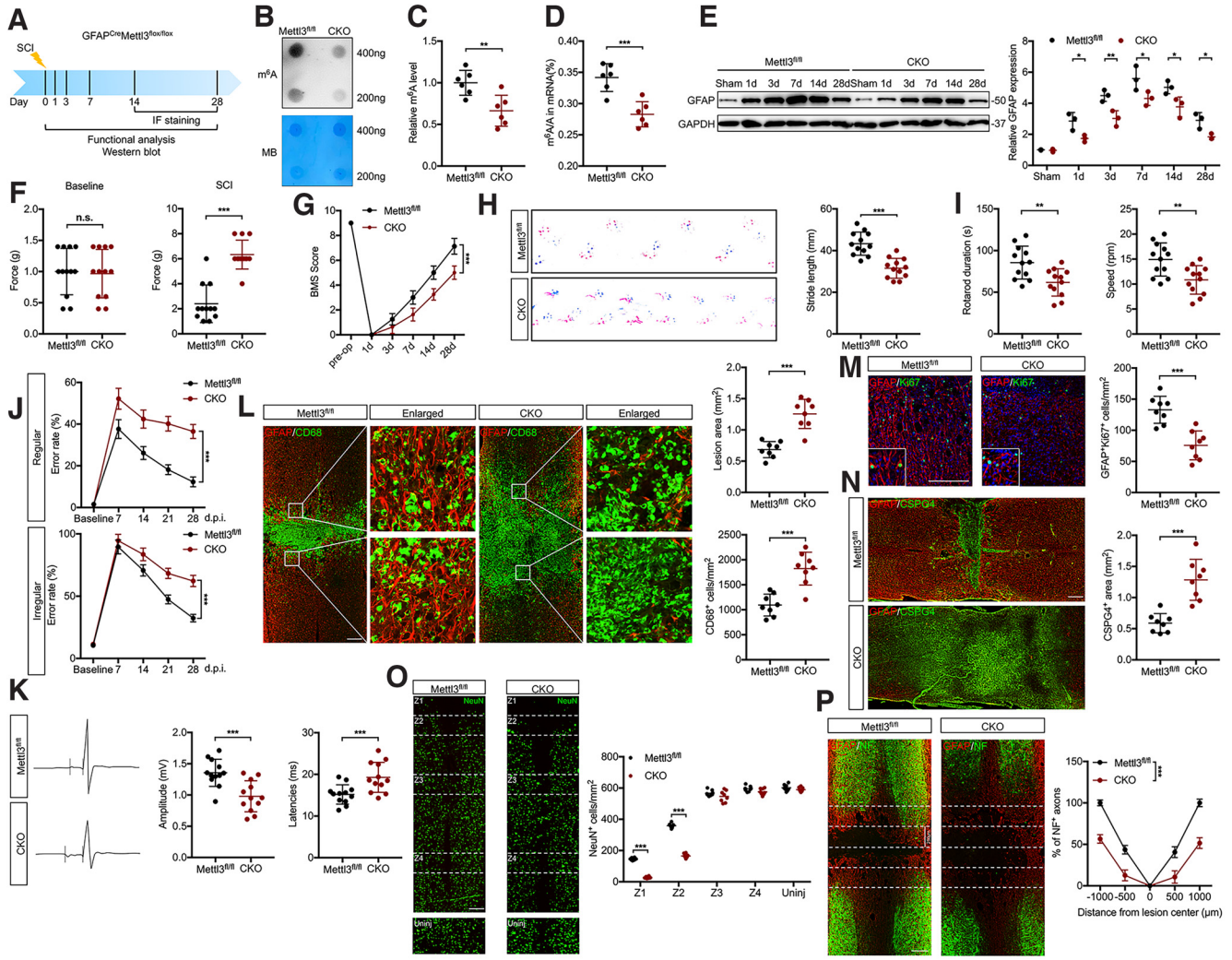

Figure 6. Conditional METTL3 deletion in astrocytes hinders functional recovery and suppresses reactive astrogliosis after SCI. ***A***, Schematic diagram of functional analysis after SCI. ***B–D***, RNA m^{6}A methylation levels of Mettl3$^{fl/fl}$ and Mettl3^{CKO} mice were evaluated by dot blot (***B***), colorimetric m^{6}A quantification assay (***C***), and LC-MS/MS assay (***D***); $^{**}p = 0.0063$, $^{***}p < 0.001$. ***E***, Protein expression and quantification of GFAP in 4 mm spinal cord centered on the lesion core of Mettl3$^{fl/fl}$ and Mettl3^{CKO} mice at the indicated times after SCI; $^{*}p < 0.05$, $^{**}p = 0.0037$. ***F***, Sensory behaviors by von Frey test of Mettl3$^{fl/fl}$ and Mettl3^{CKO} mice at baseline and day 28 postinjury; $^{***}p < 0.001$. ***G***, BMS score of Mettl3$^{fl/fl}$ and Mettl3^{CKO} mice at the indicated times following SCI; $^{***}p < 0.001$. ***H***, Footprint analysis of Mettl3$^{fl/fl}$ and Mettl3^{CKO} mice 28 d after SCI; $^{***}p < 0.001$. ***I***, Rotarod test of Mettl3$^{fl/fl}$ and Mettl3^{CKO} mice 28 d after SCI; $^{**}p < 0.01$. ***J***, Ladder walking (regular- and irregular-spaced rungs) of Mettl3$^{fl/fl}$ and Mettl3^{CKO} mice at the indicated time after SCI; $^{***}p < 0.001$. ***K***, Representative images and quantification of MEP amplitude and latencies in Mettl3$^{fl/fl}$ and Mettl3^{CKO} mice at day 28 postinjury; $^{***}p < 0.001$. ***L***, Representative immunofluorescence images of GFAP and CD68 expression and quantification of lesion area and CD68$^+$ macrophages/microglia in Mettl3$^{fl/fl}$ and Mettl3^{CKO} mice at day 14 postinjury; $^{***}p < 0.001$. ***M***, Double staining of GFAP and Ki67 and quantification of GFAP$^+$Ki67$^+$ cells in spinal cords of Mettl3$^{fl/fl}$ and Mettl3^{CKO} mice at day 14 postinjury; $^{***}p < 0.001$. ***N***, Immunofluorescence images of GFAP and CSPG4 and quantification of CSPG4$^+$ area in spinal cords of Mettl3$^{fl/fl}$ and Mettl3^{CKO} mice; $^{***}p < 0.001$. ***O***, Immunostaining of NeuN in spinal cords of Mettl3$^{fl/fl}$ and Mettl3^{CKO} mice at day 14 postinjury and quantification of viable neurons in Z1–Z4 zones adjacent to lesion boundary; $^{***}p < 0.001$. ***P***, Double staining of GFAP and NF in spinal cords of Mettl3$^{fl/fl}$ and Mettl3^{CKO} mice at day 28 postinjury and quantification of NF$^+$ axons at various distances from lesion center; $^{***}p < 0.001$. Two-way ANOVA followed by *post hoc* Bonferroni correction (***E***, ***G***, ***J***, ***O***, ***P***); Student's two-tailed unpaired *t* test (***C***, ***D***, ***F***, ***H***, ***I***, ***K***, ***L***, ***M***, ***N***). Scale bar, 200 μm.

genes were identified with $|\log_2 FC| > 1$ and $p < 0.05$ by RNA-seq, and 371 differentially m^{6}A modified genes were identified by MeRIP-seq. Only 27 genes were significantly changed in both RNA level and m^{6}A level (Fig. 7*A*), and most of m^{6}A modification was located in the coding sequence and 3′-UTR regions of mRNA (Fig. 7*B*). As expected, the most common m^{6}A motif, GGAC, was strikingly enriched in control astrocytes, but not in METTL3-knockdown astrocytes (Fig. 7*C*). Enriched gene ontology analysis further demonstrated a major enrichment in the mRNA splicing process and mitotic cell cycle (Fig. 7*D*), and KEGG analysis also revealed an enriched cell cycle pathway (Fig. 7*E*), which means METTL3 not only participates in several mRNA processes but also regulates astrocyte cell cycle. Hippo signaling pathway is widely known to participate in cell cycle regulation through nuclear transport of nonphosphorylated YAP1 (Zanconato et al., 2019). In agreement with previous studies (Xie et al., 2020), YAP1 was upregulated and activated following SCI (Fig. 7*F*,*G*) and *in vitro* astrocytic scratch injury (Fig. 7*H*,*I*). The expression of previously described proliferative YAP1 target genes was mostly upregulated at days 1 and 3 after SCI (Klatt Shaw et al., 2021; Fig. 7*J*,*K*). Intriguingly, METTL3 depletion considerably downregulated *YAP1* m^{6}A level as well as its mRNA expression (Fig. 7*L*). Moreover, abundant m^{6}A sites were mostly located in the 3′-UTR region of *YAP1* mRNA, and METTL3 ablation remarkably decreased its m^{6}A peaks (Fig. 7*M*). Notably, the binding of *YAP1* transcript and m^{6}A or METTL3 protein was validated by RIP assay (Fig. 7*N*,*O*), and METTL3 knockdown significantly reduced

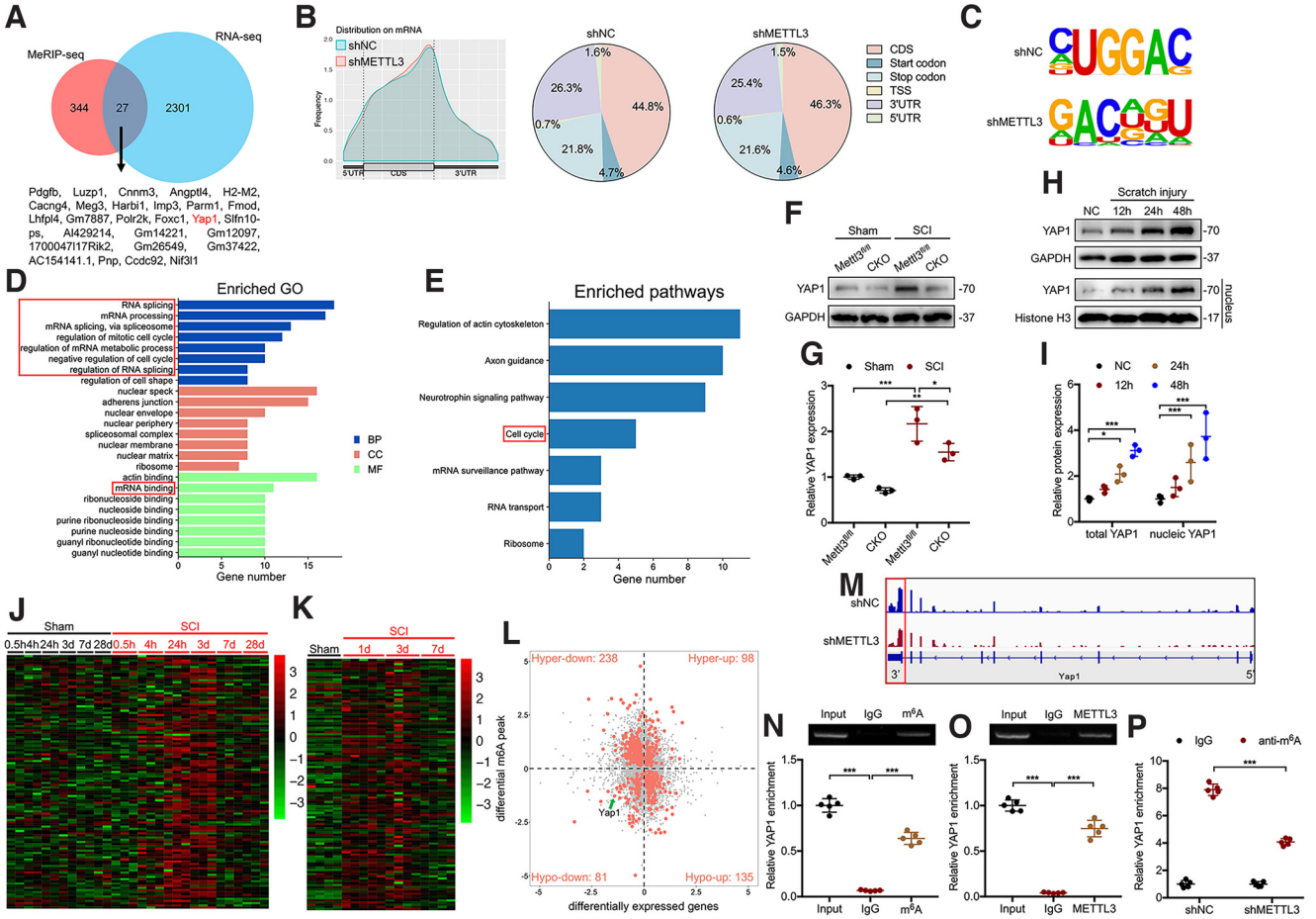

Figure 7. *YAP1* is a potential target of METTL3 in astrocytes. ***A***, Venn plot of different genes in MeRIP-seq and RNA-seq comparing primary astrocytes with or without METTL3 depletion. ***B***, M^{6}A peak distribution in indicated regions of primary astrocytes with or without METTL3 depletion. ***C***, M^{6}A motif of astrocytes with or without METTL3 silencing. ***D***, Gene ontology analysis of differentially m^{6}A modified genes following METTL3 knockdown. ***E***, KEGG analysis of differentially expressed genes after METTL3 depletion. ***F***, ***G***, Expression and quantification of YAP1 in Mettl3$^{fl/fl}$ and Mettl3^{CKO} mice with or without injury; $*p = 0.047$, $**p = 0.0083$, $***p = 0.0010$. ***H***, ***I***, Expression and quantification of astrocytic total and nucleic YAP1 at indicated times after scratch injury; $*p = 0.0145$, $***p < 0.001$. ***J***, ***K***, Heat maps of a set of proliferative YAP1 target genes in GSE5296 (***J***) and GSE42828 (***K***). ***L***, Volcano plot of genes with a significant change in both m^{6}A level and gene expression level after METTL3 silencing. ***M***, The abundance of m^{6}A sites in *YAP1* mRNA of primary astrocytes with or without METTL3 ablation. ***N***, MeRIP-PCR analysis of primary astrocytes precipitated with anti-m^{6}A and then evaluated by real-time PCR of *YAP1*; $***p < 0.001$. ***O***, RIP-PCR analysis of primary astrocytes precipitated with anti-METTL3 and then evaluated by real-time PCR of *YAP1*; $***p < 0.001$. ***P***, MeRIP-qPCR analysis of control and METTL3 knockdown astrocytes precipitated with anti-m^{6}A, and subsequently probed with *YAP1*; $***p < 0.001$. One-way ANOVA followed by *post hoc* Bonferroni correction (***G***, ***I***, ***N***, ***O***); two-way ANOVA followed by *post hoc* Bonferroni correction (***P***). Data of MeRIP sequence comparing astrocytes with or without METTL3 depletion are shown in Extended Data Figure 7-1.

m^{6}A-precipitated *YAP1* mRNA level (Fig. 7*P*). Collectively, these data indicate that *YAP1* transcript might be a target of METTL3 in reactive astrogliosis.

METTL3 regulates the stability of *YAP1* mRNA in an IGF2BP2-dependent manner

Next, we performed a series of experiments to further evaluate the effects of METTL3 on *YAP1* expression. METTL3 ablation markedly attenuated astrocytic *YAP1* mRNA expression (Fig. 8*A*), as well as protein level and nuclear localization (Fig. 8*B*). *In vivo*, METTL3 CKO attenuated total YAP1 protein level in both sham and injured spinal cord (Fig. 7*F*,*G*). Of note, the half-life of *YAP1* mRNA after transcription inhibition was shortened in METTL3-knockdown astrocytes (Fig. 8*C*). Conversely, METTL3 overexpression significantly enhanced YAP1 expression, whereas addition of 3-deazaadenosine (DAA; a global methylation inhibitor; catalog #HY-W013332, MedChem Express) reversed this effect (Fig. 8*D*,*E*). A luciferase reporter system fused with the 3′-UTR region of the *YAP1* transcript was constructed and transfected into primary astrocytes to further confirm how METTL3 regulation affects *YAP1* (Fig. 8*F*). Luciferase activity of the WT *YAP1*-3′-UTR-fused reporter was abated on METTL3 depletion, whereas knockdown of METTL3 showed no effects on the mutant with all GGAC sequence in 3′-UTR region mutated (Fig. 8*G*). Because the YAP1 protein is highly susceptible to ubiquitin modification and subjected to proteasome degradation (Liu et al., 2020; Zhou et al., 2020), we then investigated whether METTL3 could regulate the YAP1 ubiquitination process. Following protein translation blocking with 10 µg/ml CHX, METTL3 silencing did not influence the degradation rate of YAP1 protein (Fig. 8*H*). Moreover, ubiquitination of YAP1 remained unchanged after METTL3 knockdown in astrocytes (Fig. 8*I*), and METTL3 knockout also showed no effects on YAP1 ubiquitination *in vivo* (Fig. 8*J*). These results indicate that METTL3 could regulate *YAP1* expression by maintaining its mRNA stability.

Indeed, m^{6}A modified mRNAs are subsequently recognized and bound by readers, which mediate the stability, transport, and translation process of mRNA. To determine the participation of readers in the regulation of *YAP1* transcript stability, we then calculated the correlation coefficient between *YAP1* and all

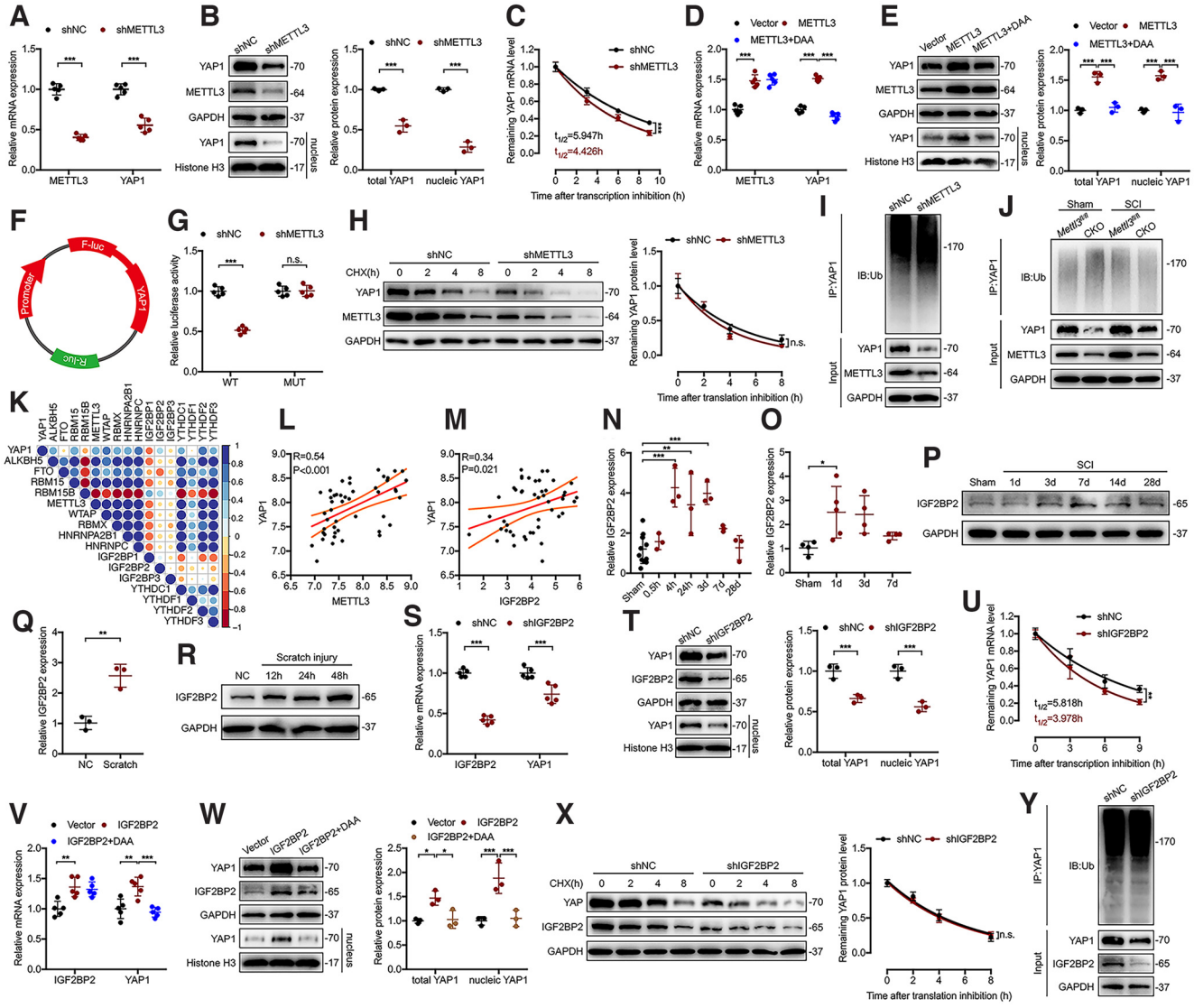

Figure 8. METTL3 regulates the stability of YAP1 mRNA in an IGF2BP2-dependent manner. ***A***, Relative mRNA expression of astrocytic *YAP1 and METTL3* following METTL3 knockdown; ***$p < 0.001$. ***B***, Expression and quantification of total YAP1 and nucleic YAP1 after METTL3 silencing; ***$p < 0.001$. ***C***, Half-life of astrocytic *YAP1* mRNA with or without METTL3 depletion was evaluated by RT-qPCR; ***$p < 0.001$. ***D***, Relative mRNA level of YAP1 after METTL3 overexpression with or without 1 μM methylation inhibitor treatment for 24 h; ***$p < 0.001$. ***E***, Expression and quantification of total YAP1 and nucleic YAP1 after METTL3 overexpression with or without 1 μM methylation inhibitor treatment for 24 h; ***$p < 0.001$. ***F***, Schematic diagram of luciferase reporter plasmid. ***G***, Effects of METTL3 knockdown on luciferase activity of astrocytes transfected with WT or *YAP1* m^{6}A sites mutated luciferase reporter plasmid; ***$p < 0.001$. ***H***, Half-life of astrocytic *YAP1* protein with or without METTL3 depletion was evaluated and quantified by Western blotting; $p = 0.2615$. ***I***, Ubiquitination levels of YAP1 protein in control and METTL3-silenced astrocytes were detected by Co-IP analysis. ***J***, Ubiquitination levels of YAP1 protein in Mettl3$^{fl/fl}$ and Mettl3^{CKO} mice with or without SCI were examined by Co-IP. ***K–M***, Correlation analysis between *YAP1* and m^{6}A-related genes based on GSE5296 and GSE42828. ***N***, ***O***, Relative mRNA expressions of *IGF2BP2* in GSE5296 (***N***) and GSE42828 (***O***); *$p = 0.047$, **$p = 0.0013$, ***$p < 0.001$. ***P***, Expression of IGF2BP2 protein at the indicated times after SCI was detected by Western blot. ***Q***, Relative mRNA expression of *IGF2BP2* in RNA sequence of scratch-injured astrocytes; **$p = 0.0035$. ***R***, Expression of astrocytic IGF2BP2 protein at the indicated times after scratch injury. ***S***, Relative mRNA expression of astrocytic *YAP1 and IGF2BP2* following IGF2BP2 knockdown; ***$p < 0.001$. ***T***, Expression and quantification of total YAP1 and nucleic YAP1 after IGF2BP2 silencing; ***$p < 0.001$. ***U***, Half-life of astrocytic *YAP1* mRNA with or without IGF2BP2 depletion was evaluated by RT-qPCR. $p = 0.0045$. ***V***, Relative mRNA level of *YAP1* after IGF2BP2 overexpression with or without 1 μM methylation inhibitor treatment for 24 h; **$p < 0.01$, ***$p = 0.0008$. ***W***, Expression and quantification of total YAP1 and nucleic YAP1 after IGF2BP2 overexpression with or without 1 μM methylation inhibitor treatment for 24 h; *$p < 0.05$, ***$p < 0.001$. ***X***, Half-life of astrocytic YAP1 protein with or without METTL3 depletion was evaluated after 10 μg/ml CHX treatment and quantified by Western blotting. $p = 0.4245$. ***Y***, Ubiquitination levels of YAP1 protein in control and IGF2BP2-silenced astrocytes were detected by Co-IP assay. One-way ANOVA followed by *post hoc* Bonferroni correction (***A***, ***B***, ***D***, ***E***, ***G***, ***N***, ***O***, ***S***, ***T***, ***V***, ***W***); Two-way ANOVA followed by *post hoc* Bonferroni correction (***C***, ***H***, ***U***, ***X***); Nonlinear regression of one phase decay (***C***, ***H***, ***U***, ***X***); Student's two-tailed unpaired *t* test (***Q***); Pearson correlation analysis (***K–M***).

m^{6}A-related genes based on two aforementioned databases (Fig. 8*K*). Consistent with the above results, *METTL3* was positively correlated with *YAP1* (Fig. 8*L*). Of note, *IGF2BP2* is the only reader positively associated with *YAP1* in the IGF2BP family that generally maintains mRNA stability (Fig. 8*M*). As a type of conserved m^{6}A binding protein with four K homology domains and two RNA recognition motif domains, IGF2BP2 could enhance target transcript stability by recruiting cofactors including HuR and matrin 3 (Huang et al., 2018). Determined by RT-qPCR and Western blot analysis, expression of IGF2BP2 was upregulated after SCI (Figs. 8*N–P*, 1*E*,*F*) and by *in vitro* astrocytic scratch injury (Figs. 8*Q*,*R*, 1*L*). Similar to METTL3, silencing of IGF2BP2 significantly inhibited YAP1 expression and nuclear transport (Fig. 8*S*,*T*), and the half-life of *YAP1* transcript was

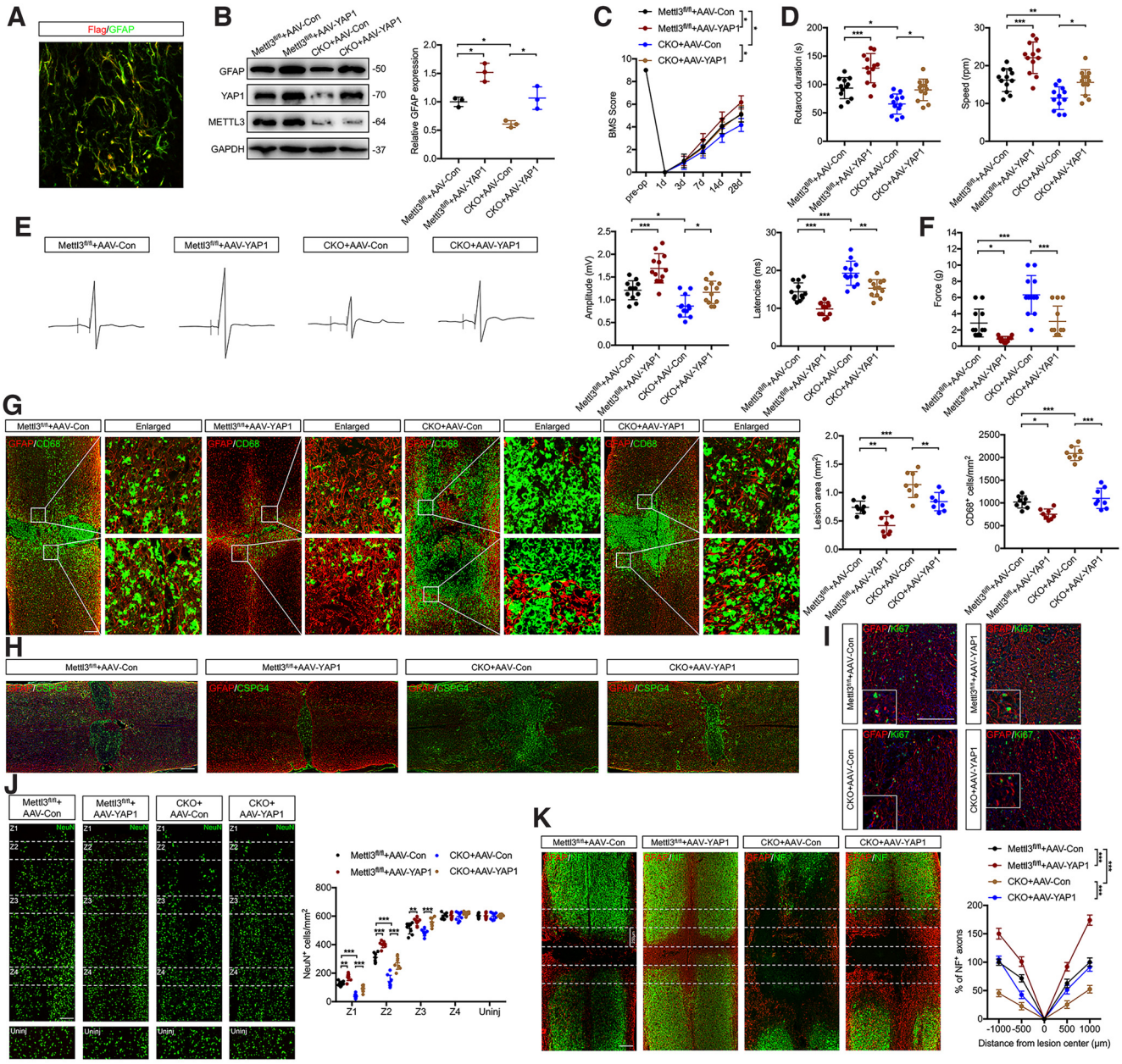

Figure 9. METTL3 promotes functional recovery and reactive astrogliosis via upregulating YAP1 expression after SCI. ***A***, Specific expression of AAV-YAP1 was verified by immunofluorescence staining GFAP and Flag. ***B***, Protein levels of GFAP, YAP1, and METTL3 in indicated groups were examined and quantified via Western blotting; $^*p < 0.05$. ***C***, BMS score of Mettl3$^{fl/fl}$ and Mettl3^{CKO} mice injected with or without AAV-YAP1 at the indicated time after SCI; $^*p < 0.05$. ***D***, Rotarod test of mice in indicated groups at day 28 postinjury; $^*p < 0.05$, $^{**}p = 0.0083$, $^{***}p < 0.001$. ***E***, Representative images and quantification of MEPs amplitude and latencies of mice in indicated groups at day 28 postinjury; $^*p < 0.05$, $^{**}p = 0.0015$, $^{***}p < 0.001$. ***F***, Sensory behaviors of mice in indicated groups at day 28 postinjury were assessed by von Frey assay; $^*p = 0.0492$, $^{***}p < 0.001$. ***G***, At day 14 postinjury, double staining of GFAP and CD68 in spinal cords of Mettl3$^{fl/fl}$ and Mettl3^{CKO} mice injected with or without AAV-YAP1 and quantification of lesion area and CD68$^+$ macrophages/microglia; $^*p = 0.0164$, $^{**}p < 0.01$, $^{***}p < 0.001$. ***H***, Immunostaining of GFAP and CSPG4 in spinal cords of the indicated groups. ***I***, Double staining of GFAP and Ki67 in spinal cords of the indicated groups at day 14 postinjury. ***J***, Immunostaining of NeuN in spinal cords of indicated groups at day 14 postinjury and quantification of viable neurons in Z1–Z4 zones adjacent to lesion boundary; $^{**}p < 0.01$, $^{***}p < 0.001$. ***K***, Double staining of GFAP and NF in spinal cords of indicated groups at day 28 postinjury and quantification of NF$^+$ axons at various distances from lesion center; $^{***}p < 0.001$. One-way ANOVA followed by *post hoc* Bonferroni correction (***B***, ***D–G***). Two-way ANOVA followed by *post hoc* Bonferroni correction (***C***, ***J***, ***K***). Scale bar, 200 μm.

shortened in IGF2BP2-knockdown astrocytes upon the transcription block (Fig. 8*U*). On the contrary, *YAP1* mRNA and protein levels as well as nuclear transport were augmented on IGF2BP2 overexpression, which could be abolished by DAA addition (Fig. 8*V*,*W*). Notably, IGF2BP2 had no influence on YAP1 protein degradation and ubiquitination in primary astrocytes (Fig. 8*X*,*Y*), indicating that IGF2BP2-mediated YAP1 expression depends on its m^{6}A modification function. Together, METTL3 could methylate the *YAP1* transcript in an IGF2BP2-dependent manner, thus suppressing its degradation.

METTL3 promotes functional recovery and reactive astrogliosis via upregulating YAP1 expression after SCI

To characterize whether METTL3 deletion-associated functional recovery inhibition following SCI is caused by regulation of YAP1, we subsequently generated YAP1-overexpressed mice by injection of astrocyte-specific AAV serotype 9 (AAV9) carrying

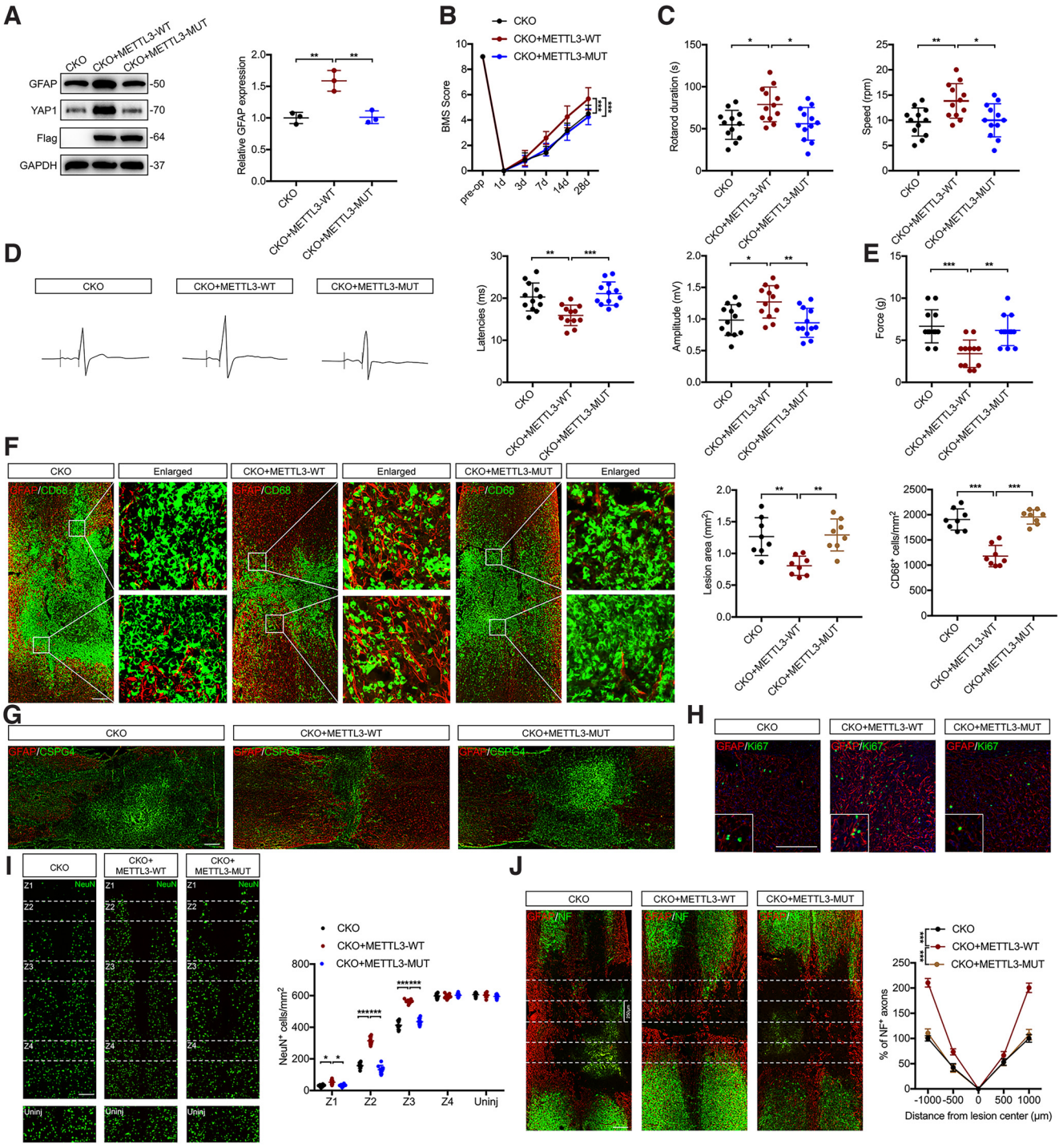

Figure 10. METTL3-mediated reactive astrogliosis and functional recovery after SCI are dependent on its m^{6}A methyltransferase function. ***A***, Protein levels of GFAP, YAP1, and Flag in indicated groups were examined and quantified by Western blotting; $^{**}p < 0.01$. ***B***, BMS score of Mettl3^{CKO} mice injected with AAV-METTL3-WT or AAV-METTL3-MUT at the indicated time after SCI; $^{***}p < 0.001$. ***C***, Rotarod test of mice in indicated groups at day 28 postinjury; $^{*}p < 0.05$, $^{**}p = 0.0087$. ***D***, Representative images and quantification of MEP amplitude and latencies of mice in indicated groups at day 28 postinjury; $^{*}p = 0.0201$, $^{**}p < 0.01$, $^{***}p = 0.0003$. ***E***, Sensory behaviors of mice in indicated groups at day 28 postinjury were assessed by von Frey assay; $^{**}p = 0.002$, $^{***}p < 0.001$. ***F***, At day 14 postinjury, double staining of GFAP and CD68 in spinal cords of Mettl3^{CKO} mice subjected to AAV-METTL3-WT or AAV-METTL3-MUT injection and quantification of lesion area and CD68$^+$ macrophages/microglia; $^{**}p < 0.01$, $^{***}p < 0.001$. ***G***, Immunostaining of GFAP and CSPG4 in spinal cords of the indicated groups. ***H***, Double staining of GFAP and Ki67 in spinal cords of the indicated groups at day 14 postinjury. ***I***, Immunostaining of NeuN in spinal cords of indicated groups at day 14 postinjury and quantification of viable neurons in Z1–Z4 zones adjacent to lesion boundary; $^{*}p < 0.05$, $^{***}p < 0.001$. ***J***, Double staining of GFAP and NF in spinal cords of indicated groups at day 28 postinjury and quantification of NF$^+$ axons at various distances from lesion center; $^{***}p < 0.001$. One-way ANOVA followed by *post hoc* Bonferroni correction (***A***, ***C–F***). Two-way ANOVA followed by *post hoc* Bonferroni correction (***B***, ***I***, ***J***). Scale bar, 200 μm.

the mouse *YAP1* sequence (AAV-YAP1) into the cranial and caudal spinal cord of the lesion site immediately after injury. Immunofluorescence staining (Fig. 9*A*) and Western blot analysis (Fig. 9*B*) identified successful transfection of AAV-YAP1 in astrocytes adjacent to the epicenter. GFAP expression was also increased in both Mettl3$^{fl/fl}$ and Mettl3^{CKO} mice subjected to AAV-YAP1 injection after SCI (Fig. 9*B*). Additionally, astrocytic YAP1 overexpression after SCI could promote METTL3

depletion-induced hindlimb functional recovery impairment (Fig. 9*C*). The motor coordination ability of Mettl3$^{fl/fl}$ and Mettl3^{CKO} mice injected with AAV-YAP1 was greatly improved, when compared with the corresponding control, as indicated by longer rotarod duration and higher speed endurance (Fig. 9*D*). Moreover, YAP1 ectopic expression significantly shortened latencies and enhanced the amplitude of mice MEPs, partly reversing METTL3 knock-out-induced deterioration of hindlimb nerve conduction function after SCI (Fig. 9*E*). In addition to motor function, AAV-YAP1 injection parallels increased mice tactile sensitivity at day 28 postinjury and remarkably abolished effects of METTL3 depletion on sensory function recovery (Fig. 9*F*). Of note, YAP1 overexpression could promote reactive astrogliosis in Mettl3^{CKO} mice after SCI, with decreased lesion areas and limited infiltration of inflammatory cells in both Mettl3$^{fl/fl}$ and Mettl3^{CKO} mice subjected to AAV-YAP1 injection, when compared with corresponding controls (Fig. 9*G*). Additionally, larger scar areas induced by METTL3 depletion were confined by YAP1 overexpression (Fig. 9*H*), and astrocyte proliferation after SCI was remarkably enhanced by AAV-YAP1 injection (Fig. 9*I*). In line with these results, METTL3 conditional knockout significantly decreased the number of viable neurons (Fig. 9*J*) and suppressed axonal sprouting (Fig. 9*K*) after SCI, whereas these effects were considerably reversed in mice with ectopic expression of YAP1 (Fig. 9*J*,*K*). Collectively, these results indicated that METTL3 promoted functional recovery and reactive astrogliosis via upregulating YAP1 expression after SCI.

METTL3-mediated reactive astrogliosis and functional recovery after SCI are dependent on its m^{6}A methyltransferase function

AAV-mediated gene therapy for SCI has become a promising approach by taking advantage of the disrupted blood–spinal cord barrier and long-term expression of target genes in specific cell types with high biosafety. To lay a crucial foundation for METTL3-targeted SCI clinical therapy and investigate whether METTL3 induced reactive astrogliosis and functional recovery after SCI depend on its m^{6}A methyltransferase function; mouse *METTL3* sequence with or without the methyltransferase domain mutated was fused in AAV9 and subsequently injected into Mettl3^{CKO} mice. As shown in Figure 10*A*, injection of AAV9 carrying WT *METTL3* (AAV-METTL3-WT) augmented expression of GFAP protein in Mettl3^{CKO} mice, and the YAP1 protein level was enhanced as well by METTL3 re-expression, whereas AAV9 with mutated *METTL3* (AAV-METTL3-MUT) failed to show these effects. As expected, CKO mice with ectopic expression of METTL3 performed much better in the BMS score with more frequent plantar stepping compared with mice with mutated METTL3 expression (Fig. 10*B*), and METTL3 re-expression significantly prolonged the time that mice remained on the rotarod, whereas mutated METTL3 expression without methyltransferase function showed no improvement in motor coordination ability (Fig. 10*C*). Moreover, hindlimb nerve conduction of CKO mice with AAV-METTL3-WT injection showed shorter latencies and larger-scale amplitude compared with AAV-METTL3-MUT injection (Fig. 10*D*). In terms of sensory function, there was a significant decrease in the tingling threshold of CKO mice re-expressing METTL3, whereas no change was observed in mice with mutated METTL3 expression (Fig. 10*E*). Notably, spinal cord double staining of GFAP and CD68 at day 14 postinjury demonstrated that reactive astrogliosis was evidently enhanced, and the infiltration of inflammatory cells was suppressed in METTL3 deletion mice subjected to AAV-METTL3-WT injection but not in mice administered with mutated METTL3 (Fig. 10*F*). Additionally, the CSPG4 expression was significantly suppressed in Mettl3^{CKO} mice with METTL3 re-expression, whereas METTL3 mutant injection showed no improvement (Fig. 10*G*). Costaining of GFAP and Ki67 demonstrated consistent results that METTL3 depletion-mediated reactive astrogliosis suppression could be rescued by re-expressing METTL3 *in vivo* but not by expressing its mutant (Fig. 10*H*). Consequently, the number of viable neurons in the Z1–Z3 zones was increased in the METTL3-WT group, whereas the methyltransferase domain mutant failed to safeguard adjacent neurons (Fig. 10*I*). Again, axonal regeneration of Mettl3^{CKO} mice could only be restored by METTL3-WT but not METTL3-MUT constructs (Fig. 10*J*). Collectively, these results demonstrated that METTL3-mediated reactive astrogliosis and functional recovery after SCI depends on its m^{6}A methyltransferase function, and METTL3 specifically delivered into astrocytes by AAV injection might become an effective therapy for future treatment of SCI.

Discussion

Epigenetic modification in SCI has been rarely studied, and the role of m^{6}A decoration in SCI has not been recognized. Recently, an altered m^{6}A methylation profile was initially reported in a zebrafish SCI model, and METTL3 was upregulated in both astrocytes and neural stem cells (Xing et al., 2021). Another study indicated METTL14 could modulate neuron apoptosis during the repair of SCI (Wang et al., 2021). Because the major location of METTL3 is in neurons, and there is a lower expression in astrocytes during nontraumatic circumstances, most studies have investigated the roles of METTL3 in neural development and axonal generation (Yoon et al., 2017; C.X. Wang et al., 2018; Yu et al., 2018). However, the specific mechanism of METTL3 upregulation and its function in SCI have never been expounded on.

Most previous studies have considered biological functions of METTL3 in downstream target regulation, whereas few have revealed the upstream modification of METTL3. A recent study demonstrated that histone lactylation increased METTL3 expression in tumor-infiltrating myeloid cells and lactylation on zinc finger domain of METTL3 enhanced its ability to capture target RNA (Xiong et al., 2022). Moreover, SUMOylation of METTL3 was confirmed to be upregulated in hepatocellular carcinoma and was positively correlated with high metastatic potential (Xu et al., 2020). Several phosphorylation sites were identified on the endogenous METTL3 protein. However, they may have no effects on METTL3 subcellular localization or binding and methylation activity (Schöller et al., 2018). Furthermore, a previous CRISPR-based screen consequently identified that USP5 could enhance METTL3 level via a deubiquitination effect, and its corresponding inhibitors significantly decreased METTL3 expression (Sun et al., 2020). Indeed, deubiquitination modification of the METTL3 protein was also reported in the viral replication process. We have demonstrated that an increasing level of m^{6}A and astrocytic METTL3 expression after SCI was mediated by the USP1/UAF1 complex, which subsequently stabilized the METTL3 protein through removing K48-linked polyubiquitination. Previous studies have already established a deep understanding of deubiquitination modification in SCI. For instance, the concentration of UCHL-1 peaks within 8 h after CNS injury, and its expression is positively correlated with the severity of SCI (Khetani et al., 2019). Augmented expression of astrocytic USP18 after SCI significantly improves functional recovery by attenuating SOX9 ubiquitination (W. Liu et al., 2021). Although USP1 expression is augmented after SCI, its biological functions and role of its stoichiometric

partner UAF1 in SCI have not been investigated. Notably, the deubiquitinase activity of USP1 could be enhanced by UAF1 in our study, and the USP1/UAF1 complex was previously reported to participate in stabilization of the NLRP3 and TBK1 proteins by hydrolyzing polyubiquitination with the K48-linkage (Yu et al., 2017; Song et al., 2020).

The crystal structure of the methyltransferase complex suggests that METTL14 only contributes to RNA binding and stabilization of the complex, whereas METTL3 is the main catalytic subunit, and WTAP plays a crucial role in recruiting METTL3 and METTL14 to nuclear speckles (Ping et al., 2014; Wang et al., 2016). Most previous studies have revealed that METTL3 regulates target transcript stability and translational efficiency. C.X. Wang et al. (2018) reported that METTL3 conditional knockout manifested cerebellar hypoplasia via enhancing stability of apoptosis-associated genes. (Zhang et al. 2018) demonstrated that METTL3 depletion markedly prolonged the process of long-term memory consolidation by impeding translation of target genes. However, functions of METTL3 in astrocytes after SCI have never been reported. Based on the combination of MeRIP-seq and RNA-seq, we have noted that METTL3 could regulate the methylation level and stability of astrocytic *YAP1* mRNA, whereas there is no influence on protein degradation. As a core kinase in the Hippo signaling pathway, YAP1 is involved in regulating cell proliferation to determine organ growth and regeneration (Misra and Irvine, 2018). Inhibition of the Hippo signaling pathway results in nuclear transport of nonphosphorylated YAP1 protein with TAZ, which subsequently controls downstream gene transcription to regulate cell fate. Klatt Shaw et al. (2021) discovered that localized YAP1 activation as well participates in reprogramming of glial progenitors to promote spinal cord repair. The decline of astrocytic LATS1 could considerably inhibit YAP1 phosphorylation and promote astrogliosis after SCI (Wang and Chen, 2018). In brains of mice with intracerebral hemorrhage, YAP1 nuclear translocation was observed in hemoglobin-activated astrocytes, which facilitated the astroglial-mesenchymal transition process (Yang et al., 2018b). However, epigenetic modification of YAP1 after SCI is still unclear. The *in vivo* and *in vitro* experiments in our study further indicated *YAP1* as a potential target of METTL3, and as expected, when mutating the methyltransferase domain of METTL3, its regulation of YAP1 protein expression was abolished, which further verified the interaction of METTL3 and *YAP1* mRNA. Indeed, m^{6}A modification of the *YAP1* transcript plays a crucial role in maintaining its stability, thus contributing to reactive astrogliosis and functional recovery after SCI.

Notably, the role of reactive astrocytes in SCI has been widely debated for a long time. Traditionally, glial scar formation and secretion of a large amount of extracellular matrix including CSPGs, fibronectin, and collagen by reactive astrocytes were regarded as a permanent barrier to regenerating axons not only mechanically but also chemically (Ahuja et al., 2017). Previous studies reported that suppressing glial scar formation could promote axonal regeneration and functional recovery after SCI (Pakulska et al., 2017). Degrading inhibitory CSPG molecules by enzyme chondroitinase can improve axonal sprouting after CNS injury (Rosenzweig et al., 2019). As a major component of inhibitory CSPG species expressed at sites of SCI, CSPG4 is highly upregulated within 24 h of injury, peaks at 1 week, and remains elevated for 2 months (Jones et al., 2002). Unlike other CSPGs, CSPG4 is typically expressed on cell membranes rather than as an extracellular matrix, leading to fibrotic and glial scar formation (Hackett and Lee, 2016; Hesp et al., 2018). However, more recently, benefits of reactive astrocytes in neural repair have been clarified as they demarcate the lesion area, secrete neurotrophic factors, and facilitate blood–spinal cord barrier reconstruction (Vivinetto et al., 2020). Conditional ablation or genetic modification of reactive astrocytes after SCI did not significantly reduce the total level of CSPGs or induce axonal regeneration but consequently led to widespread infiltration of inflammatory cells, progressive neuron loss, and failure of functional recovery, suggesting astrocyte scar formation aids rather than inhibits axonal regeneration (Okada et al., 2006; Gu et al., 2019). Some studies have even demonstrated that the glial scar functioned as a bridge to guide axonal regeneration (Anderson et al., 2016; Klatt Shaw et al., 2021). Our previous study also revealed that promoting reactive astrogliosis significantly sealed off injured tissues and limited inflammation to further safeguard surviving neurons (W. Liu et al., 2021). Moreover, astrocytes are regarded as a potential reservoir for neurogenesis, and reprogramming of astrocytes is only observed after injury (Zamboni et al., 2020). Another study also reported that reactive glia in an injured microenvironment could acquire stem cell properties in response to sonic hedgehog signaling (Sirko et al., 2013). Notably, with the increasing popularity of RNA methylation research, its role in astrocytes has been gradually described. Studies have shown that an epigenetic mechanism is involved in neural and glial differentiation of progenitor cells via a precise gene expression program. Furthermore, METTL3-mediated m^{6}A

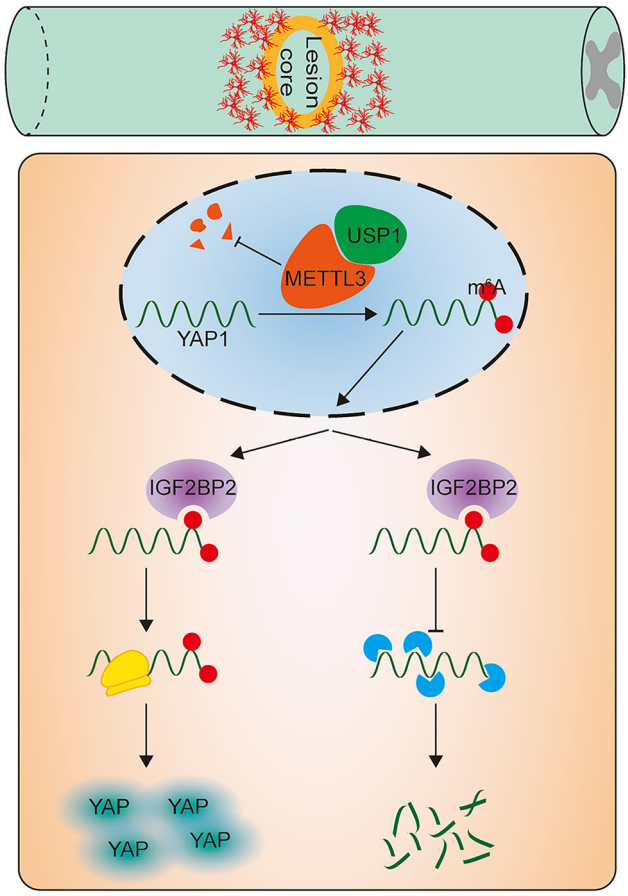

Figure 11. A schematic diagram showing the beneficial effects of METTL3 in reactive astrogliosis after SCI and the underlying mechanism. METTL3 protein is upregulated after SCI and stabilized by the USP1/UAF1 complex, thus subsequently promoting reactive astrogliosis, limiting inflammatory cell infiltration, and improving function recovery through mediating methylation and stability of *YAP1* mRNA in an IGF2BP2-dependent manner.

modification reduces astrocyte differentiation from neural stem cells with a natural preference toward neural fate (Chen et al., 2019), and knockdown of METTL3 leads to a decreased number of astrocytes in the developing cerebullum (Ma et al., 2018). Indeed, it appeared that METTL3 plays an oncogenic role in glioblastoma, and silencing METTL3 or ectopic expression of METTL3 mutants significantly inhibits growth and self-renewal of glioma stem cells. In our perspective, reactive astrogliosis mediated by the METTL3/YAP1 axis contributes to behavioral improvement after SCI.

Although still limited, targeting of METTL3 for potential clinical application has been reported recently. A structure-based screening by Selberg et al. (2019) identified four molecular ligands that bind to and serve as the activators of the methyltransferase complex, whereas its clinical application has not been reported. Recent research indicated that controlling activity of methyltransferase with small-molecule drugs holds promise for therapeutic modification of cell differentiation pathways (Meyer and Jaffrey, 2017). Zhou et al. (2022) reported that exenatide (a commonly used hypoglycemic agent in clinical practice) could inhibit pancreatic β-cell apoptosis by inducing METTL3 expression. Moreover, the association between METTL3 activity and cell survival after ultraviolet-light-induced DNA damage provides a potential therapy for ultraviolet light exposure (Xiang et al., 2017). Nowadays, rAAV targeted gene therapies have been gradually conducted in clinics, and most therapies are focused on the liver, muscle, and CNS, considering natural tropism and clinical needs (Wang et al., 2019). By taking advantage of its high biosafety and stable genetic information, and delivery into specific cell types remotely or directly, the rAAV vector has already been tested in several clinical trials of neurodegenerative disorders (Stepankova et al., 2021). However, rAAV administration in SCI treatment is still in the preclinical stage because of the uncertain effects of gene transfer in human patients. In our study, rAAV carrying the *METTL3* sequence significantly improved functional recovery after SCI via promoting reactive astrogliosis-induced neuroinflammation amelioration and axonal regeneration, which might provide a novel insight for METTL3-targeted rAAV therapy for patients with SCI in the foreseeable future.

To conclude, our work revealed that the METTL3 protein is upregulated after SCI and stabilized by the USP1/UAF1 complex, thus subsequently promoting reactive astrogliosis, limiting inflammatory cells infiltration, and improving functional recovery through modulating methylation and stability of the *YAP1* transcript in an IGF2BP2-dependent manner (Fig. 11).

References

Ahuja CS, Wilson JR, Nori S, Kotter MRN, Druschel C, Curt A, Fehlings MG (2017) Traumatic spinal cord injury. Nat Rev Dis Primers 3:17018.

Anderson MA, Burda JE, Ren YL, Ao Y, O'Shea TM, Kawaguchi R, Coppola G, Khakh BS, Deming TJ, Sofroniew MV (2016) Astrocyte scar formation aids central nervous system axon regeneration. Nature 532:195–200.

Chen J, Zhang YC, Huang C, Shen H, Sun B, Cheng X, Zhang YJ, Yang YG, Shu Q, Yang Y, Li X (2019) m(6)A regulates neurogenesis and neuronal development by modulating histone methyltransferase Ezh2. Genomics Proteomics Bioinformatics 17:154–168.

Ge X, et al. (2021) Exosomal miR-155 from M1-polarized macrophages promotes EndoMT and impairs mitochondrial function via activating NF-κB signaling pathway in vascular endothelial cells after traumatic spinal cord injury. Redox Biol 41:101932.

Grice GL, Nathan JA (2016) The recognition of ubiquitinated proteins by the proteasome. Cell Mol Life Sci 73:3497–3506.

Gu YK, Cheng XY, Huang X, Yuan YM, Qin SY, Tan ZJ, Wang D, Hu X, He C, Su ZD (2019) Conditional ablation of reactive astrocytes to dissect their roles in spinal cord injury and repair. Brain Behav Immun 80:394–405.

Hackett AR, Lee JK (2016) Understanding the NG2 glial scar after spinal cord injury. Front Neurol 7:199.

Hesp ZC, Yoseph RY, Suzuki R, Jukkola P, Wilson C, Nishiyama A, McTigue DM (2018) Proliferating NG2-cell-dependent angiogenesis and scar formation alter axon growth and functional recovery after spinal cord injury in mice. J Neurosci 38:1366–1382.

Huang H, et al. (2018) Recognition of RNA N(6)-methyladenosine by IGF2BP proteins enhances mRNA stability and translation. Nat Cell Biol 20:285–295.

Huang J, Dong X, Gong Z, Qin LY, Yang S, Zhu YL, Wang X, Zhang D, Zou T, Yin P, Tang C (2019) Solution structure of the RNA recognition domain of METTL3-METTL14 N(6)-methyladenosine methyltransferase. Protein Cell 10:272–284.

James ND, McMahon SB, Field-Fote EC, Bradbury EJ (2018) Neuromodulation in the restoration of function after spinal cord injury. Lancet Neurol 17:905–917.

Jiang D, Gong F, Ge X, Lv C, Huang C, Feng S, Zhou Z, Rong Y, Wang J, Ji C, Chen J, Zhao W, Fan J, Liu W, Cai W (2020) Neuron-derived exosomes-transmitted miR-124-3p protect traumatically injured spinal cord by suppressing the activation of neurotoxic microglia and astrocytes. J Nanobiotechnology 18:105.

Jones LL, Yamaguchi Y, Stallcup WB, Tuszynski MH (2002) NG2 is a major chondroitin sulfate proteoglycan produced after spinal cord injury and is expressed by macrophages and oligodendrocyte progenitors. J Neurosci 22:2792–2803.

Khetani S, Kollath VO, Eastick E, Debert C, Sen A, Karan K, Sanati-Nezhad A (2019) Single-step functionalization of poly-catecholamine nanofilms for ultra-sensitive immunosensing of ubiquitin carboxyl terminal hydrolase-L1 (UCHL-1) in spinal cord injury. Biosens Bioelectron 145:111715.

Klatt Shaw D, Saraswathy VM, Zhou L, McAdow AR, Burris B, Butka E, Morris SA, Dietmann S, Mokalled MH (2021) Localized EMT reprograms glial progenitors to promote spinal cord repair. Dev Cell 56:613–626.e7.

Kumar R, Lim J, Mekary RA, Rattani A, Dewan MC, Sharif SY, Osorio-Fonseca E, Park KB (2018) Traumatic spinal injury: global epidemiology and worldwide volume. World Neurosurg 113:E345–E363.

Lence T, Akhtar J, Bayer M, Schmid K, Spindler L, Ho CH, Kreim N, Andrade-Navarro MA, Poeck B, Helm M, Roignant JY (2016) m(6)A modulates neuronal functions and sex determination in *Drosophila*. Nature 540:242–247.

Li K, Nicaise C, Sannie D, Hala TJ, Javed E, Parker JL, Putatunda R, Regan KA, Suain V, Brion JP, Rhoderick F, Wright MC, Poulsen DJ, Lepore AC (2014) Overexpression of the astrocyte glutamate transporter GLT1 exacerbates phrenic motor neuron degeneration, diaphragm compromise, and forelimb motor dysfunction following cervical contusion spinal cord injury. J Neurosci 34:7622–7638.

Li X, Li M, Tian L, Chen J, Liu R, Ning B (2020) Reactive astrogliosis: implications in spinal cord injury progression and therapy. Oxid Med Cell Longev 2020:9494352.

Lin XY, Chai GS, Wu YM, Li JX, Chen F, Liu JZ, Luo GZ, Tauler J, Du J, Lin SB, He C, Wang HS (2019) RNA m(6)A methylation regulates the epithelial mesenchymal transition of cancer cells and translation of Snail. Nat Commun 10:2065.

Liu B, Ruan J, Chen M, Li Z, Manjengwa G, Schluter D, Song W, Wang X (2021) Deubiquitinating enzymes (DUBs): decipher underlying basis of neurodegenerative diseases. Mol Psychiatry 27:259–268.

Liu M, Yan M, Lv H, Wang B, Lv X, Zhang H, Xiang S, Du J, Liu T, Tian Y, Zhang X, Zhou F, Cheng T, Zhu Y, Jiang H, Cao Y, Ai D (2020) Macrophage K63-linked ubiquitination of YAP promotes its nuclear localization and exacerbates atherosclerosis. Cell Rep 32:107990.

Liu W, Ge X, Zhou Z, Jiang D, Rong Y, Wang J, Ji C, Fan J, Yin G, Cai W (2021) Deubiquitinase USP18 regulates reactive astrogliosis by stabilizing SOX9. Glia 69:1782–1798.

Ma C, Chang M, Lv H, Zhang ZW, Zhang W, He X, Wu G, Zhao S, Zhang Y, Wang D, Teng X, Liu C, Li Q, Klungland A, Niu Y, Song S, Tong WM (2018) RNA m(6)A methylation participates in regulation of postnatal development of the mouse cerebellum. Genome Biol 19:68.

Meyer KD, Jaffrey SR (2014) The dynamic epitranscriptome: N6-methyladenosine and gene expression control. Nat Rev Mol Cell Biol 15:313–326.

Meyer KD, Jaffrey SR (2017) Rethinking m(6)A readers, writers, and erasers. Annu Rev Cell Dev Biol 33:319–342.

Misra JR, Irvine KD (2018) The hippo signaling network and its biological functions. Annu Rev Genet 52:65–87.

Okada S, Nakamura M, Katoh H, Miyao T, Shimazaki T, Ishii K, Yamane J, Yoshimura A, Iwamoto Y, Toyama Y, Okano H (2006) Conditional ablation of Stat3 or Socs3 discloses a dual role for reactive astrocytes after spinal cord injury. Nat Med 12:829–834.

Pakulska MM, Tator CH, Shoichet MS (2017) Local delivery of chondroitinase ABC with or without stromal cell-derived factor 1α promotes functional repair in the injured rat spinal cord. Biomaterials 134:13–21.

Pappalardo LW, Samad OA, Black JA, Waxman SG (2014) Voltage-gated sodium channel Nav 1.5 contributes to astrogliosis in an *in vitro* model of glial injury via reverse Na+/Ca2+ exchange. Glia 62:1162–1175.

Patil DP, Chen CK, Pickering BF, Chow A, Jackson C, Guttman M, Jaffrey SR (2016) m(6)A RNA methylation promotes XIST-mediated transcriptional repression. Nature 537:369–373.

Pekny M, Pekna M (2014) Astrocyte reactivity and reactive astrogliosis: costs and benefits. Physiol Rev 94:1077–1098.

Ping XL, et al. (2014) Mammalian WTAP is a regulatory subunit of the RNA N6-methyladenosine methyltransferase. Cell Res 24:177–189.

Rosenzweig ES, et al. (2019) Chondroitinase improves anatomical and functional outcomes after primate spinal cord injury. Nat Neurosci 22:1269–1275.

Schöller E, Weichmann F, Treiber T, Ringle S, Treiber N, Flatley A, Feederle R, Bruckmann A, Meister G (2018) Interactions, localization, and phosphorylation of the m(6)A generating METTL3-METTL14-WTAP complex. RNA 24:499–512.

Selberg S, Blokhina D, Aatonen M, Koivisto P, Siltanen A, Mervaala E, Kankuri E, Karelson M (2019) Discovery of small molecules that activate RNA methylation through cooperative binding to the METTL3-14-WTAP complex active site. Cell Rep 26:3762–3771.e5.

Shen C, Xuan B, Yan T, Ma Y, Xu P, Tian X, Zhang X, Cao Y, Ma D, Zhu X, Zhang Y, Fang JY, Chen H, Hong J (2020) m(6)A-dependent glycolysis enhances colorectal cancer progression. Mol Cancer 19:72.

Shi HL, Wei JB, He C (2019) Where, when, and how: context-dependent functions of RNA methylation writers, readers, and erasers. Mol Cell 74:640–650.

Sirko S, et al. (2013) Reactive glia in the injured brain acquire stem cell properties in response to sonic hedgehog. [corrected]. Cell Stem Cell 12:426–439.

Śledź P, Jinek M (2016) Structural insights into the molecular mechanism of the m(6)A writer complex. Elife 5:e18434.

Song H, Zhao C, Yu Z, Li Q, Yan R, Qin Y, Jia M, Zhao W (2020) UAF1 deubiquitinase complexes facilitate NLRP3 inflammasome activation by promoting NLRP3 expression. Nat Commun 11:6042.

Stepankova K, Jendelova P, Machova Urdzikova L (2021) Planet of the AAVs: the spinal cord injury episode. Biomedicines 9:613.

Sun HL, Zhu AC, Gao Y, Terajima H, Fei Q, Liu S, Zhang L, Zhang Z, Harada BT, He YY, Bissonnette MB, Hung MC, He C (2020) Stabilization of ERK-Phosphorylated METTL3 by USP5 Increases m(6)A Methylation. Mol Cell 80:633–647.e7.

Tran AP, Warren PM, Silver J (2018) The biology of regeneration failure and success after spinal cord injury. Physiol Rev 98:881–917.

Vivinetto AL, Kim ID, Goldberg DC, Fones L, Brown E, Tarabykin VS, Hill CE, Cho S, Cave JW (2020) Zeb2 is a regulator of astrogliosis and functional recovery after CNS injury. Cell Rep 31:107834.

Wang CX, Cui GS, Liu XY, Xu K, Wang M, Zhang XX, Jiang LY, Li A, Yang Y, Lai WY, Sun BF, Jiang GB, Wang HL, Tong WM, Li W, Wang XJ, Yang YG, Zhou Q (2018) METTL3-mediated m(6) A modification is required for cerebellar development. Plos Biol 16:e2004880.

Wang D, Tai PWL, Gao G (2019) Adeno-associated virus vector as a platform for gene therapy delivery. Nat Rev Drug Discov 18:358–378.

Wang H, Yuan J, Dang X, Shi Z, Ban W, Ma D (2021) Mettl14-mediated m6A modification modulates neuron apoptosis during the repair of spinal cord injury by regulating the transformation from pri-mir-375 to miR-375. Cell Biosci 11:52.

Wang X, Feng J, Xue Y, Guan Z, Zhang D, Liu Z, Gong Z, Wang Q, Huang J, Tang C, Zou T, Yin P (2016) Structural basis of N(6)-adenosine methylation by the METTL3-METTL14 complex. Nature 534:575–578.

Wang Y, Chen M (2018) Decreased expression of LATS1 correlates with astrogliosis after spinal cord injury. Biochem Biophys Res Commun 505:151–156.

Wang Y, Li Y, Yue MH, Wang J, Kumar S, Wechsler-Reya RJ, Zhang ZL, Ogawa Y, Kellis M, Duester G, Zhao JC (2018) N-6-methyladenosine RNA modification regulates embryonic neural stem cell self-renewal through histone modifications. Nat Neurosci 21:1139–1139.

Wanner IB, Anderson MA, Song B, Levine J, Fernandez A, Gray-Thompson Z, Ao Y, Sofroniew MV (2013) Glial scar borders are formed by newly proliferated, elongated astrocytes that interact to corral inflammatory and fibrotic cells via STAT3-dependent mechanisms after spinal cord injury. J Neurosci 33:12870–12886.

Xiang Y, Laurent B, Hsu CH, Nachtergaele S, Lu Z, Sheng W, Xu C, Chen H, Ouyang J, Wang S, Ling D, Hsu PH, Zou L, Jambhekar A, He C, Shi Y (2017) RNA m(6)A methylation regulates the ultraviolet-induced DNA damage response. Nature 543:573–576.

Xie C, et al. (2020) Astrocytic YAP promotes the formation of glia scars and neural regeneration after spinal cord injury. J Neurosci 40:2644–2662.

Xing LY, Cai YY, Yang T, Yu WW, Gao MD, Chai R, Ding SJ, Wei JH, Pan JY, Chen G (2021) Epitranscriptomic m6A regulation following spinal cord injury. J Neurosci Res 99:843–857.

Xiong J, He J, Zhu J, Pan J, Liao W, Ye H, Wang H, Song Y, Du Y, Cui B, Xue M, Zheng W, Kong X, Jiang K, Ding K, Lai L, Wang Q (2022) Lactylation-driven METTL3-mediated RNA m(6)A modification promotes immunosuppression of tumor-infiltrating myeloid cells. Mol Cell 82:1660–1677.e10.

Xu F, Li JJ, Ni MD, Cheng JY, Zhao HY, Wang SS, Zhou X, Wu XH (2021) FBW7 suppresses ovarian cancer development by targeting the N-6-methyladenosine binding protein YTHDF2. Mol Cancer 20:45.

Xu H, Wang H, Zhao W, Fu S, Li Y, Ni W, Xin Y, Li W, Yang C, Bai Y, Zhan M, Lu L (2020) SUMO1 modification of methyltransferase-like 3 promotes tumor progression via regulating snail mRNA homeostasis in hepatocellular carcinoma. Theranostics 10:5671–5686.

Yang Y, Hsu PJ, Chen YS, Yang YG (2018a) Dynamic transcriptomic m(6)A decoration: writers, erasers, readers and functions in RNA metabolism. Cell Res 28:616–624.

Yang Y, Ren J, Sun Y, Xue Y, Zhang Z, Gong A, Wang B, Zhong Z, Cui Z, Xi Z, Yang GY, Sun Q, Bian L (2018b) A connexin43/YAP axis regulates astroglial-mesenchymal transition in hemoglobin induced astrocyte activation. Cell Death Differ 25:1870–1884.

Yoon K-J, Ringeling FR, Vissers C, Jacob F, Pokrass M, Jimenez-Cyrus D, Su Y, Kim N-S, Zhu Y, Zheng L, Kim S, Wang X, Doré LC, Jin P, Regot S, Zhuang X, Canzar S, He C, Ming G-L, Song H (2017) Temporal control of mammalian cortical neurogenesis by m(6)A methylation. Cell 171:877–889.e17.

Yu J, Chen M, Huang H, Zhu J, Song H, Zhu J, Park J, Ji SJ (2018) Dynamic m6A modification regulates local translation of mRNA in axons. Nucleic Acids Res 46:1412–1423.

Yu Z, Song H, Jia M, Zhang J, Wang W, Li Q, Zhang L, Zhao W (2017) USP1-UAF1 deubiquitinase complex stabilizes TBK1 and enhances antiviral responses. J Exp Med 214:3553–3563.

Zaccara S, Ries RJ, Jaffrey SR (2019) Reading, writing and erasing mRNA methylation. Nat Rev Mol Cell Biol 20:608–624.

Zamboni M, Llorens-Bobadilla E, Magnusson JP, Frisen J (2020) A widespread neurogenic potential of neocortical astrocytes is induced by injury. Cell Stem Cell 27:605–617.e5.

Zanconato F, Cordenonsi M, Piccolo S (2019) YAP and TAZ: a signalling hub of the tumour microenvironment. Nat Rev Cancer 19:454–464.

Zeng C, Huang W, Li Y, Weng H (2020) Roles of METTL3 in cancer: mechanisms and therapeutic targeting. J Hematol Oncol 13:117.

Zhang C, Wang Y, Peng Y, Xu H, Zhou X (2020) METTL3 regulates inflammatory pain by modulating m(6)A-dependent pri-miR-365-3p processing. FASEB J 34:122–132.

Zhang Z, Wang M, Xie D, Huang Z, Zhang L, Yang Y, Ma D, Li W, Zhou Q, Yang YG, Wang XJ (2018) METTL3-mediated N(6)-methyladenosine mRNA modification enhances long-term memory consolidation. Cell Res 28:1050–1061.

Zhao BXS, Wang X, Beadell AV, Lu ZK, Shi HL, Kuuspalu A, Ho RK, He C (2017) m(6)A-dependent maternal mRNA clearance facilitates zebrafish maternal-to-zygotic transition. Nature 542:475–478.

Zhou S, Sun Y, Xing Y, Wang Z, Wan S, Yao X, Hua Q, Meng X, Cheng J, Zhong M, Lv K, Kong X (2022) Exenatide ameliorates hydrogen peroxide-induced pancreatic β-cell apoptosis through regulation of METTL3-mediated m(6)A methylation. Eur J Pharmacol 924:174960.

Zhou Y, Zhang J, Li H, Huang T, Wong CC, Wu F, Wu M, Weng N, Liu L, Cheng ASL, Yu J, Wong N, Lo KW, Tang PMK, Kang W, To KF (2020) AMOTL1 enhances YAP1 stability and promotes YAP1-driven gastric oncogenesis. Oncogene 39:4375–4389.